

High-resolution regional gravity field modelling in a mountainous area from terrestrial gravity data

Blažej Bucha,¹ Juraj Janák,¹ Juraj Papčo¹ and Aleš Bezděk²

¹Department of Theoretical Geodesy, Faculty of Civil Engineering, Slovak University of Technology in Bratislava, Radlinského 11, 81005 Bratislava, Slovak Republic. E-mail: blazej.bucha@gmail.com

²Astronomical Institute, Czech Academy of Sciences, Fričova 298, 25165 Ondřejov, Czech Republic

Accepted 2016 August 12. Received 2016 July 1; in original form 2016 May 2

SUMMARY

We develop a high-resolution regional gravity field model by a combination of spherical harmonics, band-limited spherical radial basis functions (SRBFs) and the residual terrain model (RTM) technique. As the main input data set, we employ a dense terrestrial gravity database ($3\text{--}6$ stations km^{-2}), which enables gravity field modelling up to very short spatial scales. The approach is based on the remove–compute–restore methodology in which all the parts of the signal that can be modelled are removed prior to the least-squares adjustment in order to smooth the input gravity data. To this end, we utilize degree-2159 spherical harmonic models and the RTM technique using topographic models at 2 arcsec resolution. The residual short-scale gravity signal is modelled via the band-limited Shannon SRBF expanded up to degree 21 600, which corresponds to a spatial resolution of 30 arcsec. The combined model is validated against GNSS/levelling-based height anomalies, independent surface gravity data, deflections of the vertical and terrestrial vertical gravity gradients achieving an accuracy of 2.7 cm, 0.53 mGal, 0.39 arcsec and 279 E in terms of the RMS error, respectively. A key aspect of the combined approach, especially in mountainous areas, is the quality of the RTM. We therefore compare the performance of two RTM techniques within the innermost zone, the tesserae and the polyhedron. It is shown that the polyhedron-based approach should be preferred in rugged terrain if a high-quality RTM is required. In addition, we deal with the RTM computations at points located below the reference surface of the residual terrain which is known to be a rather delicate issue.

Key words: Numerical solutions; Inverse theory; Geopotential theory.

1 INTRODUCTION

In recent years, significant progress has been made in gravity field modelling at very short spatial scales. One of the major breakthroughs was certainly due to the EGM2008 model (Pavlis *et al.* 2012), which approximates the Earth's gravity signal down to about 9 km resolution. EGM2008 is a global spherical-harmonic-based model complete to degree and order 2159 and contains additional coefficients up to degree 2190 and order 2159. Examples of other up-to-date high-resolution models are EIGEN-6C4 (Förste *et al.* 2014) and GECO (Gilardoni *et al.* 2016), which are derived mainly from EGM2008 and some additional satellite data to improve the long and medium wavelengths. Though the ~ 9 km resolution may suffice for some global applications, demands on regional gravity field knowledge are often far beyond this scale. Particularly, high-resolution (beyond degree 2159) regional gravity modelling becomes inevitable in mountainous areas, as the very short wavelengths, uncovered by the high-degree spherical harmonic models,

are correlated with local topography to a large extent. It is expected that the missing signal can reach from ~ 3 to 23 mGals ($1 \text{ mGal} = 10^{-5} \text{ m s}^{-2}$) in terms of gravity anomaly degree variances (see table 4 in Rexer & Hirt 2015a), depending on the roughness of the topography. Local extrema are typically much larger. In rugged terrain, spherical harmonic models are therefore often supplemented with high-frequency gravity information implied by the local (residual) topography using a residual terrain model (RTM; Forsberg 1984). For instance, in a numerical test conducted in the German Alps, Hirt *et al.* (2010) have shown that adding the RTM-implied signal reduces the RMS error of the EGM2008-based height anomalies by about 50 per cent. In the case of deflections of the vertical, Hirt (2010) reported an improvement rate of ~ 75 per cent in mountainous test areas (the German and the Swiss Alps).

Despite the promising results achieved with high-degree harmonic models along with the RTM technique, the main limiting factor of this combination is obvious. In practice, the RTM method cannot deliver the true high-frequency gravity signal, owing to the

(usually) assumed constant density of topographic masses. This assumption is made out of necessity, since an accurate density distribution of topographic masses is rarely available. As a consequence, geological structures beyond the spatial resolution of the spherical harmonic model still remain uncovered. To achieve further improvements, the residual short-scale signal needs to be taken mainly from terrestrial data whose signal power is rich in high harmonic degrees, for example, gravity, deflections of the vertical or vertical gravity gradients. This can be done in the remove–compute–restore fashion. The terrestrial observations, reduced by a high-degree spherical harmonic model and RTM data, can be inverted into a residual field. The residual component then supplements the RTM-implied signal—which is based on the constant mass-density assumption—with information derived from real gravity data reflecting the actual density inhomogeneities. Such a model is therefore capable of a much better approximation of the true gravity signal and can be used in geophysical investigations up to very short spatial scales. It is, however, implicitly presupposed that the spatial distribution of the observations is dense enough to recover the short-scale signal, since the maximum recoverable harmonic degree is related to the spatial resolution of observations (e.g. Sneeuw 1994; Blais *et al.* 2006). For instance, the gravity field up to degree 21 600 is recoverable if, among some other conditions, input data are given at a global grid with an equiangular spacing of at least 30 arcsec. To model the residual component of the gravity field, we employ spherical radial basis functions (SRBFs).

For several decades, starting probably in the 1960s (e.g. Weightman 1967; Krarup 1969), SRBFs have been widely used to model the gravity field, especially on a regional scale. SRBFs are kernel functions given on a sphere which depend only on the spherical distance between two points on this sphere (Freeden & Schreiner 2009). Limiting ourselves to recent terrestrial gravity applications, we mention some of the SRBF-based techniques: for example, free-positioned point-masses (e.g. Claessens *et al.* 2001; Lin *et al.* 2014), the Poisson kernel (e.g. Klees *et al.* 2008; Tenzer & Klees 2008) or wavelets and splines (e.g. Kuroishi & Keller 2005; Schmidt *et al.* 2007; Wittwer 2009; Panet *et al.* 2011; Tenzer *et al.* 2012; Pock *et al.* 2014). In general, SRBF-based techniques can compete with other gravity field modelling techniques, for example, spherical harmonics (e.g. Bucha *et al.* 2015) or geoid modelling via the Stokes formula (e.g. Klees *et al.* 2008), but also provide some additional advantages. For instance, more than 466 millions of coefficients need to be determined when expanding the gravity field up to degree 21 600 in terms of spherical harmonics. Though this can be done by some numerically stable algorithms (e.g. Gruber *et al.* 2011; Balmino *et al.* 2012; Rexer & Hirt 2015b), it is impractical to model the regional short-scale gravity field via basis functions with global support (see e.g. Schmidt *et al.* 2007; Eicker 2008). Another drawback is that while some parts of the Earth's surface are well-surveyed by terrestrial gravity data, their resolution on the global scale is currently not sufficient to reach such high degrees. These limitations of spherical harmonics are discussed several times in the literature (e.g. Freeden & Windheuser 1997; Jekeli 2005). Under some approximations, both issues can be circumvented by a combination of spherical harmonics and, for example, SRBFs. The former is used to model the global gravity field up to some degree n_{\max} and the latter to represent the remaining upper part of the spectrum on the regional scale. The approximation errors are due to the omitted far-zone contributions in the regional model for degrees beyond n_{\max} . By this combination, both the number of expansion coefficients can vastly be reduced, depending on the size of the recovery area, and the short-scale gravity information from local

dense gravimetric data can improve global models. In mountainous areas, the RTM method plays a key role, as it smooths the input terrestrial observations which is important for the least-squares fit. As for the comparison with the classical numerical evaluation of geodetic integrals, for example, geoid modelling via the Stokes formula, SRBFs allow to model the gravity field similarly as spherical harmonics do. From a set of expansion coefficients, one can derive commonly used functionals of the geopotential. On the contrary, geodetic integrals transform an input quantity onto an output one. Thus, when changing the output quantity, a new numerical integration has to be performed.

In this paper, we develop a regional gravity field model over the Slovak Republic (Central Europe) by means of degree-2159 harmonic models, the RTM technique and a SRBF-based approach to model the residual part from terrestrial gravity data. The topography over this region is rough (see Fig. 1) which makes it a challenging task to obtain a high-quality regional model. Moreover, in this region, terrestrial gravity measurements are dense enough ($3-6$ stations km^{-2} , in some regions even more) to model the gravity field up to degrees as high as 21 600. These circumstances provide a good opportunity to perform high-resolution regional gravity field modelling via a combination of spherical harmonics and SRBFs. We employ the final model to compute the gravitational potential, the gravitational vector and also the full gravitational tensor, from which commonly used gravity field quantities can easily be obtained. These outputs will serve as a basis for further geodetic and geophysical applications within this region. In Section 2, we provide an overview of gravity field modelling in terms of SRBFs. An attention is also paid to RTM computations, especially at the problematic points located below the reference surface. Data used to estimate and to validate the model are described in Section 3. In Section 4, we present the results and evaluate the model against GNSS/levelling-based height anomalies, independent gravity data, astrogeodetic deflections of the vertical and terrestrial vertical gravity gradients.

2 REGIONAL GRAVITY FIELD MODELING

2.1 Gravity field representation by means of spherical radial basis functions

SRBFs are kernel functions defined on a reference sphere Ω_R , with R being the radius of the sphere, depending only on the spherical distance between two points on this sphere, \mathbf{r} and \mathbf{r}_i . The point $\mathbf{r}_i \in \Omega_R$ is called the nodal point and the SRBF is rotationally symmetric around the axis represented by the direction of the unit vector $\mathbf{r}_i / |\mathbf{r}_i|$. The evaluation point \mathbf{r} can be located on the sphere Ω_R or in its exterior Ω_R^{ext} , that is, $\mathbf{r} \in \Omega_R^{\text{ext}}$, where $\Omega_R^{\text{ext}} = \Omega_R \cup \Omega_R^{\text{ext}}$. If $\mathbf{r} \in \Omega_R^{\text{ext}}$, then the SRBF is harmonically upward continued. The sphere Ω_R is completely inside the Earth and is called the Bjerhammar sphere (e.g. Moritz 1980; Klees *et al.* 2008).

The Earth's external gravitational potential V can be expressed as a series of SRBFs

$$V(\mathbf{r}) = \sum_{i=1}^I a_i \Phi(\mathbf{r}, \mathbf{r}_i), \quad (1)$$

where $\Phi(\mathbf{r}, \mathbf{r}_i)$ is a SRBF to which an expansion coefficient a_i corresponds and I is the total number of SRBFs. Here we focus on the estimation of the expansion coefficients a_i from observed gravity field quantities like gravity disturbances, height anomalies,

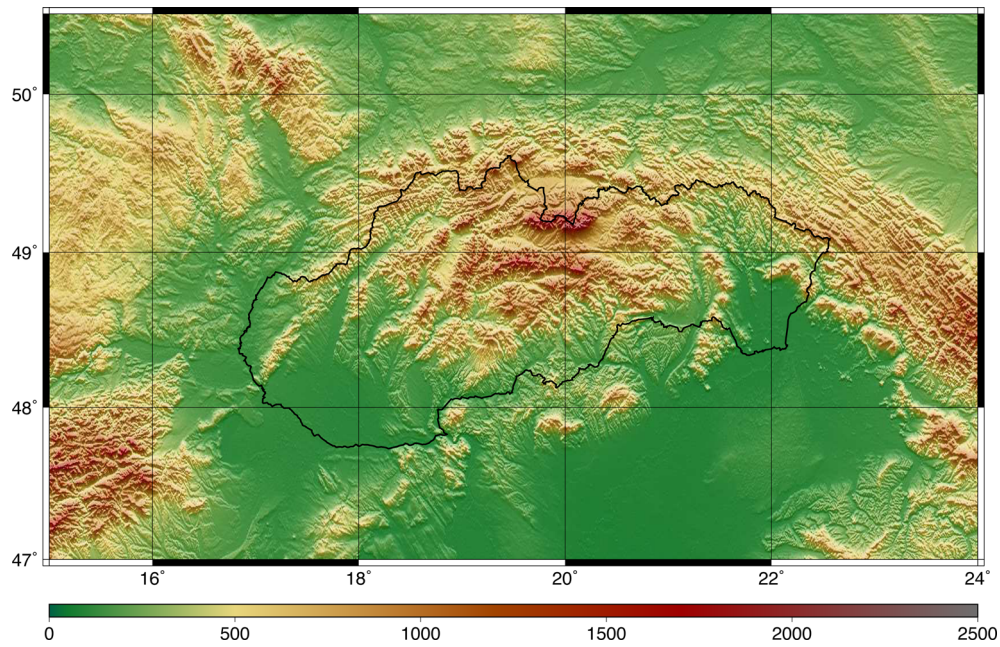


Figure 1. Topography (m) over the Slovak Republic (Central Europe) and its neighbourhood.

astrogeodetic deflections of the vertical, etc. Once the expansion coefficients are obtained, each gravity field parameter can be derived from eq. (1), similarly as in the spherical harmonics case. In eq. (1), the gravitational potential V is understood as an approximation of the true gravitational potential V^{true} in the sense of the Runge–Krarup theorem (e.g. Krarup 1969; Freedén & Schneider 1998).

We define the SRBF as (Freedén & Schneider 1998)

$$\Phi(\mathbf{r}, \mathbf{r}_i) = \sum_{n=n_{\min}}^{n_{\max}} \frac{2n+1}{4\pi R^2} \phi_n \left(\frac{R}{r} \right)^{n+1} P_n(\cos \psi), \quad (2)$$

where P_n is unnormalized Legendre polynomial of degree n , ϕ_n is the shape coefficient, $r = |\mathbf{r}|$, $\cos \psi = (\mathbf{r} \cdot \mathbf{r}_i)/(|\mathbf{r}| |\mathbf{r}_i|)$, and n_{\min} and n_{\max} are minimum and maximum degrees of the expansion, respectively. The shape coefficients ϕ_n determine the properties of SRBFs in both the spatial and spectral domain. The SRBF in eq. (2) is band-limited, since the shape coefficients are zero for each degree beyond n_{\max} . The shape coefficients of non-band-limited SRBFs do not vanish for infinitely many degrees. An overview of commonly used SRBFs can be found, for example, in Schmidt *et al.* (2007) or Klees *et al.* (2008).

We use the Shannon SRBF defined by the shape coefficients $\phi_n = 1$ for all $n = n_{\min}, \dots, n_{\max}$. The Shannon SRBF is the reproducing kernel of the space spanned by all solid spherical harmonics of degrees $n = n_{\min}, \dots, n_{\max}$ and of all corresponding orders (e.g. Freedén & Schneider 1998). As a consequence, it does not smooth the gravity signal in this spectral band. Moreover, global gravity field modelling with the Shannon SRBF leads to the same results as with spherical harmonics both in theory (see e.g. eqs 16–19 in Bentel *et al.* 2013b) and in practice (Bucha *et al.* 2015). The Shannon-based models can therefore directly be compared with spherical harmonic solutions and allow a straightforward interpretation of their discrepancies. SRBFs whose non-zero shape coefficients are not constant might smooth some gravity field harmonics, depending on the shape coefficients. Though these harmonics are present in the recovered signal, they might be significantly suppressed. One

has to be therefore careful when interpreting results based on these SRBFs, sometimes also called the smoothing kernels (e.g. Naeimi *et al.* 2015).

Besides the Shannon SRBF, one frequently employs SRBFs derived from degree variances of the Earth's gravitational potential (e.g. Eicker *et al.* 2014; Bucha *et al.* 2015; Naeimi *et al.* 2015). The degree variances can be obtained from spherical harmonic models of the gravitational potential or from some empirical rule, for example, the one by Kaula (1966) or a more recent one by Rexer & Hirt (2015a). Since these types of SRBFs are based on the degree variances, hence on some gravity data, they can be understood as *a priori* information, or, in a more general sense, as another data set. The gravity information in the degree variances should ensure that their spectral properties correspond to the spectral properties of the actual gravity field, thus avoiding a suppression of individual gravity field harmonics. In practice, this is frequently not true, especially in the case of the empirical rules, since they are only a rough approximation (see e.g. Bucha *et al.* 2015). At any rate, these types of SRBFs are not relevant for our purposes. As explained in Section 1, we work with a residual gravity field, that is, with the gravity field reduced by the contributions from the normal gravity field, a high-degree spherical harmonic model and RTM data. The spectral properties of the residual field definitely do not correspond to the degree variances derived from some spherical harmonic model or from the frequently applied empirical rules. The Shannon SRBF seems to be therefore a reasonable choice.

In our experiments, the nodal points $\mathbf{r}_i \in \Omega_R$ are arranged in the Reuter grid (e.g. Reuter 1982; Eicker 2008; Wittwer 2009). Many other grid types can be found in the literature, for example, Driscoll & Healy (1994), Freedén *et al.* (1998), Eicker (2008) or Naeimi (2013). Given a positive integer α , Reuter's algorithm generates a system of points $\mathbf{r}_i \in \Omega_R$. In the process of the gravity field determination, we use $\alpha = n_{\max} + 1$, where n_{\max} is the maximum degree of the series expansion (see eq. 2). A discussion on this empirical rule can be found, for example, in Schmidt *et al.* (2005).

2.2 Parameter estimation

We use terrestrial gravity data to estimate the residual part of the regional gravity field. The gravity vector is related to the gravitational potential in eq. (1) as follows

$$\mathbf{g}(\mathbf{r}) = \nabla V(\mathbf{r}) + \mathbf{g}_c = \sum_{i=1}^I a_i \nabla \Phi(\mathbf{r}, \mathbf{r}_i) + \mathbf{g}_c, \quad (3)$$

where \mathbf{g}_c is the vector of the centrifugal acceleration. We obtain the vector $\nabla \Phi(\mathbf{r}, \mathbf{r}_i)$ in the local north-oriented frame (LNOF; e.g. Koop & Stelpstra 1989), but other choices are possible, too (e.g. the Earth-fixed frame, Eicker 2008). In spherical approximation (the radial component of eq. 3 expressed in the LNOF), we have

$$g(\mathbf{r}) = |\mathbf{g}(\mathbf{r})| \approx - \sum_{i=1}^I a_i \frac{\partial \Phi(\mathbf{r}, \mathbf{r}_i)}{\partial r} - g_{c,z}. \quad (4)$$

This approximation, however, is unsatisfactory in view of today's accuracy requirements and at least the ellipsoidal effect has to be considered. This can be done, for example, by a rotation of eq. (3) into the LNOF aligned with the ellipsoidal normal instead of the spherical radius (see e.g. fig. 1 in Sebera *et al.* 2013). Hereafter, we use the notation LNOF^e and LNOF^s to distinguish between the ellipsoidal and spherical LNOF, respectively. In the LNOF^e, the negative value of the Z-component of the gravity vector is much closer to $g(\mathbf{r})$. The remaining discrepancies are due to the small differences in the direction of the gravity vector and of the ellipsoidal normal. The angle between the two is represented by the deflection of the vertical and, in most practical applications, can safely be neglected (for, e.g. 30 arcsec, the difference in gravity is ~ 0.01 mGal). Optionally, it can be predicted at each gravity station using high-degree spherical harmonic models together with the RTM technique. In that case, eq. (3) can further be rotated into the LNOF aligned with (an approximation of) the actual gravity vector, hereafter denoted as LNOF^g. In the computations to be presented in Section 4, we also employ the predicted deflections of the vertical, though this step is arguably unnecessary. It may, however, become essential when dealing with high-quality terrestrial gravity data in rough terrain.

To rotate the right-hand side of eq. (3) from the LNOF^s into the LNOF^g, all three components of $\nabla \Phi(\mathbf{r}, \mathbf{r}_i)$ have to be computed for each gravity station. After the rotation, an observation equation can be set up for the Z-component of the rotated vector $\nabla \Phi(\mathbf{r}, \mathbf{r}_i)$ (the X- and Y-components of $\mathbf{g}(\mathbf{r})$ are zero by definition in the LNOF^g). This, however, is inefficient from the numerical point of view. Instead, the observations $g(\mathbf{r})$ in eq. (4) can be projected onto the radial direction, and thus only the radial part of the vector $\nabla \Phi(\mathbf{r}, \mathbf{r}_i)$ (in the LNOF^s) needs to be computed. The radial projection of the gravity $g(\mathbf{r})$ is here denoted as $g_r(\mathbf{r})$. Note that prior to the projection, the atmospheric effect (see e.g. Moritz 1980) is added to the gravity $g(\mathbf{r})$.

After the term $g_r(\mathbf{r})$ is obtained, we transform it into a residual gravity disturbance

$$\delta g_r^{\text{res}}(\mathbf{r}) = g_r(\mathbf{r}) - \gamma_r(\mathbf{r}) - \delta g_r^{\text{SH}}(\mathbf{r}) - g_r^{\text{RTM}}(\mathbf{r}), \quad (5)$$

where $\gamma_r(\mathbf{r})$, $\delta g_r^{\text{SH}}(\mathbf{r})$ and $g_r^{\text{RTM}}(\mathbf{r})$ are, respectively, negative values of the radial component of the normal gravity vector, of the gravity disturbance vector synthesized from a spherical harmonic model and of the RTM-implied gravitational vector. The observation equation for the residual gravity disturbance is

$$\delta g_r^{\text{res}}(\mathbf{r}) = - \sum_{i=1}^I a_i \frac{\partial \Phi(\mathbf{r}, \mathbf{r}_i)}{\partial r} + e \quad (6)$$

with e being the observation error. Note that the coefficients a_i now represent the residual gravity field. In vector-matrix form, eq. (6) reads

$$\mathbf{y} = \mathbf{A} \mathbf{x} + \mathbf{e}, \quad (7)$$

where \mathbf{y} is the vector of residual gravity disturbances, \mathbf{A} is the design matrix, \mathbf{x} is the vector of expansion coefficients and \mathbf{e} is the error vector.

When dealing with data sets of various quality and/or combining different types of observations (e.g. gravity disturbances with height anomalies), the vector \mathbf{y} may be split into separate observation groups, each accompanied by their covariance matrix. If available, cross-correlations between the observation groups can also be taken into account. Assuming uncorrelated residual gravity disturbances split into o observation groups, we obtain the final linear model

$$\begin{aligned} \begin{bmatrix} \mathbf{y}_1 \\ \vdots \\ \mathbf{y}_o \end{bmatrix} &= \begin{bmatrix} \mathbf{A}_1 \\ \vdots \\ \mathbf{A}_o \end{bmatrix} \mathbf{x} + \begin{bmatrix} \mathbf{e}_1 \\ \vdots \\ \mathbf{e}_o \end{bmatrix}, \\ E \left\{ \begin{bmatrix} \mathbf{e}_1 \\ \vdots \\ \mathbf{e}_o \end{bmatrix} \right\} &= \mathbf{0}, D \left\{ \begin{bmatrix} \mathbf{y}_1 \\ \vdots \\ \mathbf{y}_o \end{bmatrix} \right\} = \begin{bmatrix} \sigma_1^2 \mathbf{I} & \mathbf{0} & \mathbf{0} & \cdots \\ \mathbf{0} & \sigma_2^2 \mathbf{I} & \mathbf{0} & \cdots \\ \vdots & \vdots & \ddots & \vdots \\ \mathbf{0} & \mathbf{0} & \cdots & \sigma_o^2 \mathbf{I} \end{bmatrix}, \end{aligned} \quad (8)$$

where σ_p^2 , $p = 1, \dots, o$, is (unknown) variance factor of the p th observation group, \mathbf{I} are identity matrices of corresponding dimensions, and E and D denote the expectation and dispersion operators, respectively. The variance factors σ_p^2 allow for a proper individual weighting of observation groups. The design matrix in the linear model (8) is ill-conditioned (e.g. Bentel *et al.* 2013a), thus a regularization is necessary to obtain a numerically stable solution. We achieve this by applying the Tikhonov regularization (Tikhonov & Arsenin 1977). To estimate the optimum regularization parameter and the variances factors σ_p^2 , we use the variance component estimation approach (Koch & Kusche 2002).

2.3 Residual terrain modelling

The RTM technique is based on gravity forward modelling of residual terrain, which is obtained after subtracting some reference topography from a digital topographic model (DTM), see Fig. 2. The reference topography can effectively be represented by some topographic model based on spherical harmonics, for example, DTM2006.0 (Pavlis *et al.* 2007). The reason is that topographic spherical harmonic models enable to control the spectral content of RTM data by truncating their series expansion at some degree n_{\max} . This is especially useful when combining the RTM technique with spherical-harmonic-based gravity field models. The gravity field model is responsible for the signal in harmonic degrees up to n_{\max} ,

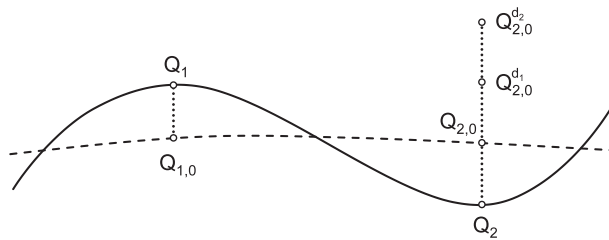


Figure 2. Digital topographic model (solid line) and reference topography (dashed line).

while the RTM data approximate the missing upper part of the spectrum. It should be, however, stressed that, in a rigorous sense, this augmentation is not valid and therefore is subject to approximation errors; see for example, Hirt *et al.* (2010) or Hirt *et al.* (2014). According to the estimate provided by Hirt *et al.* (2010), the approximation errors for height anomalies are expected to be below 10 per cent of the RTM-implied signal. Throughout the paper, we use the RTM method under the assumption of constant mass-density ($\rho = 2670 \text{ kg m}^{-3}$).

In regional gravity field modelling, the role of local topography (and thus of the RTM) in the vicinity of computation points is essential, because the gravity signal near the Earth's surface is strongly correlated with the innermost topography. For instance, Sansò & Sideris (2013) show in table 8.8 that observed gravity anomalies can be smoothed by ~ 60 per cent in terms of the standard deviation after removing the contribution from a high-degree spherical harmonic model (in this case EGM2008) and by ~ 75 per cent when further including the RTM-implied signal. The impact of local topography is even more crucial for gravity gradients. Jekeli & Zhu (2006) claim that '90 per cent of the gravitational gradient signal resides in wavelengths shorter than several hundreds of metres (after accounting for the Earth's ellipsoidal bulk)'.

In order to obtain a high-quality RTM, we approximate the topographic masses by a combination of tesseroids (Grombein *et al.* 2013) and a polyhedron (Tsoulis 2012). In general, the tesseract-based approach is faster, but approximates rough terrain less accurately than the polyhedron one and *vice versa*. Having in mind the strong impact of the innermost topography on the gravity, we divided the integration domain into a far zone and a near zone. The contribution from the far zone is obtained via the efficient tesseroids, while the near-zone effect is computed by the more accurate polyhedron. In Section 4, we also show the differences between the near-zone effect obtained via the polyhedron and the tesseroids with a horizontal subdivision as proposed by Grombein *et al.* (2013).

Next, we deal with the RTM computations at the problematic points located below the reference topography RT . This issue happens if the computation point Q is placed at the DTM and $h^{\text{DTM}} < h^{\text{RT}}$, where h is the ellipsoidal height of the point. In this case, the computation point Q is located within the topographic masses, as represented by the reference topography, where their implied gravitational potential is a non-harmonic function. Several approaches to cope with this issue can be found in the literature: for example, harmonic correction by Forsberg (1984) or harmonic continuation by Elhabiby *et al.* (2009) and Omang *et al.* (2012). A comparison of the two methods can be found in Omang *et al.* (2012). We follow the harmonic continuation approach, but compute the vertical derivatives, which are necessary for the harmonic continuation, in a different way than in the previously mentioned studies. While Omang *et al.* (2012) used the least-squares collocation, we apply the numerical differentiation. Note that the topographic potential also does not fulfil Laplace's equation at the topographic surface, but this can be solved in practice by using the actual height of the observation point Q above the terrain, here represented by the DTM.

In the following, we demonstrate the method via the gravitational potential only, but the same principle holds for each element of the gravitational vector and tensor. We assume two points, Q_1 and Q_2 , located outside and inside the reference topography, respectively (see Fig. 2). The RTM gravitational potential V^{RTM} is given as the difference between the gravitational potential implied by the DTM and by the reference topography,

$$V^{\text{RTM}}(Q_j) = V^{\text{DTM}}(Q_j) - V^{\text{RT}}(Q_j), \quad (9)$$

where $j = 1, 2$. The potential values $V^{\text{DTM}}(Q_1)$, $V^{\text{DTM}}(Q_2)$ and $V^{\text{RT}}(Q_1)$ can be computed using standard gravity forward modelling techniques, while a special treatment is needed to get the potential $V^{\text{RT}}(Q_2)$ satisfying Laplace's equation. The harmonic potential V^{RT} at both Q_1 and Q_2 can be obtained by a harmonic continuation using a Taylor series,

$$\tilde{V}^{\text{RT}}(Q_j) = \sum_{k=0}^{\infty} \frac{1}{k!} \left. \frac{\partial^k V^{\text{RT}}}{\partial r^k} \right|_{Q_{j,0} \in (RT+\epsilon)} \Delta r^k, \quad (10)$$

where Δr is the radial distance between the points Q_j and $Q_{j,0}$.

It is important to emphasize that, in a rigorous sense, the second- and higher-order radial derivatives in eq. (10) are not defined at $Q_{j,0} \in RT$ due to the density discontinuity. Without loss of generality, this issue can be solved by radially upward shifting all the points $Q_{j,0}$ by a small distance from RT to some $RT + \epsilon$, say a few metres, where V^{RT} is a harmonic function, and thus infinitely differentiable. Then, the Taylor series converges to the harmonically upward/downward continued potential \tilde{V}^{RT} . For $j = 1$, the harmonically upward continued potential $\tilde{V}^{\text{RT}}(Q_1)$ is equal to the value $V^{\text{RT}}(Q_1)$ obtained directly via the gravity forward modelling techniques which is a consequence of the harmonicity of V^{RT} outside the reference topography. Therefore, $V^{\text{RT}}(Q_1)$ can be computed using the standard approaches and only $V^{\text{RT}}(Q_2)$ needs to be obtained using the harmonic continuation approach.

The value $\tilde{V}^{\text{RT}}(Q_2)$ does not represent the gravitational potential inside the topographic masses, where Poisson's equation is valid, but rather its harmonic continuation, possessing no physical meaning, which satisfies Laplace's equation instead. This situation is very similar to the computation of the gravitational potential inside topographic masses (e.g. on some parts of the reference ellipsoid) from the usual spherical harmonic models. This procedure also results in a downward continued Earth's external gravitational potential. In fact, the approach proposed in the previous paragraph can be explained in terms of spherical harmonics as well. The gravitational potential due to a topographic spherical harmonic model can be derived using the approach by Hirt & Kuhn (2014), obtaining a spherical harmonic expansion of the topography-implied gravitational potential. This series expansion yields the effect of the entire topographic masses around the globe, that is, an integration over a whole reference sphere is implicitly assumed. To obtain the inner-zone effect only, the integration beyond some spherical distance can be prevented with the help of truncation coefficients (see e.g. Sjöberg & Hunegnaw 2000). In this way, the harmonic potential V^{RT} can alternatively be obtained at both Q_1 and Q_2 . A numerical investigation of this possible approach is, however, beyond the scope of this paper and remains a subject of future work.

We note that the Taylor series expansion can directly be applied to the value V^{RTM} . We prefer V^{RT} , since it is usually much smoother than V^{RTM} , and thus we expect that the radial derivatives can be estimated more accurately. However, no numerical tests have been conducted to verify this assumption.

As for the practical numerical computation, we approximate the radial derivatives in eq. (10) by numerical differentiation using the scheme by Fornberg (1988). The scheme generates weights to compute derivatives of any order from arbitrarily spaced samples in 1-D (here in the radial direction). The gravitational potential due to the reference topography expanded to degree $n_{\max} = 2159$ is a rather smooth function. Our numerical experiments, conducted within the area of the Slovak Republic, suggest that the Taylor series can be truncated at $k = 1$. We approximate the first-order radial derivative using the values of V^{RT} evaluated at the points $Q_{j,0}$, $Q_j^{d_1}$ and $Q_j^{d_2}$,

where d_1 and d_2 denote distances by which the point $Q_{j,0}$ is radially shifted upward, see Fig. 2. Note that to approximate $\partial V^{\text{RT}}/\partial r$ at $Q_{j,0}$, V^{RT} needs to be known at two points only, $Q_{j,0}$ and some $Q_j^{d_1}$. It should also be mentioned that $\partial V^{\text{RT}}/\partial r$ can directly be computed using gravity forward modelling techniques, for example, the tesseroids or the polyhedron. However, the third- and possibly higher-order radial derivatives—necessary to continue, for example, the gravitational tensor—are rarely discussed in the literature from the gravity forward modelling point of view. The proposed scheme might therefore be useful. We use $d_1 = 100$ m and $d_2 = 200$ m. These settings, however, should not be understood as some general rule and further tests should be carried out, especially in a more rugged region (e.g. the Himalayas) and/or with $n_{\max} > 2159$ (e.g. 10 800; see Hirt & Rexer 2015). If the reference topography is very rough, the higher-order radial derivatives can easily be obtained following the scheme by Fornberg (1988). Naturally, this requires a larger number of values V^{RT} in the radial direction which results in a longer computation time.

2.4 Numerical implementation

High-resolution regional gravity field modelling via SRBFs often leads to several tens of thousands of expansion coefficients that need to be determined. To handle such a large system of linear equations, we use the high-performance computing cluster at the Slovak University of Technology in Bratislava. Furthermore, we employ a Monte-Carlo technique by Kusche (2003) to avoid the inversion of the normal matrix. To accelerate the computation of the summation in eq. (2), we apply the Clenshaw summation (see e.g. Clenshaw 1955; Tscherning & Poder 1982; Fantino & Casotto 2009). The parallel computation technique is applied to the SRBF synthesis as well as to the RTM computations. The term $\gamma_r(\mathbf{r})$ in eq. (5) is obtained after a rotation of the normal gravity vector from the Earth-fixed frame into the LNOF^s. The normal gravity vector in the Earth-fixed frame is computed via Hotine's equation according to Sebera *et al.* (2013). All computations were carried out in Matlab. The routine `polyhedron.f`, written in Fortran by Tsoulis (2012), has been compiled as a Matlab MEX-function.

3 DATA

We use three main input data types.

(i) *Gravity data.* Three terrestrial gravity data sets, here denoted as GD1, GD2 and GD3, are used (see Fig. 3). The GD1 database (Kubeš *et al.* 2001) consists of 211 631 observations (3–6 stations km^{-2}) with an expected accuracy of ~ 0.1 – 0.2 mGal. The quality of the GD1 data set may vary regionally which is a consequence of the rather large time span during which it has been gathered (the late 1950s to the early 1990s). The gravity data in GD2, comprising a total of 107 416 stations, originate from geophysical explorations performed since the mid-1970s. The accuracy of GD2 is expected to be about 0.1 mGal. Both GD1 and GD2 have been re-processed by Paštka *et al.* (2014). The third database, GD3 (Val'ko *et al.* 2008), is a compiled grid of gravity disturbances within the area of Central Europe with the step of 20 and 30 arcsec in ellipsoidal latitude and longitude, respectively. Over the Slovak Republic, this grid is derived from the GD1 database. The gravity information beyond the borders is based on mean Bouguer gravity anomalies, whose quality, unfortunately, is poor (~ 2 mGal). We utilize the GD3 database to reduce edge effects, that is, only the grid points outside

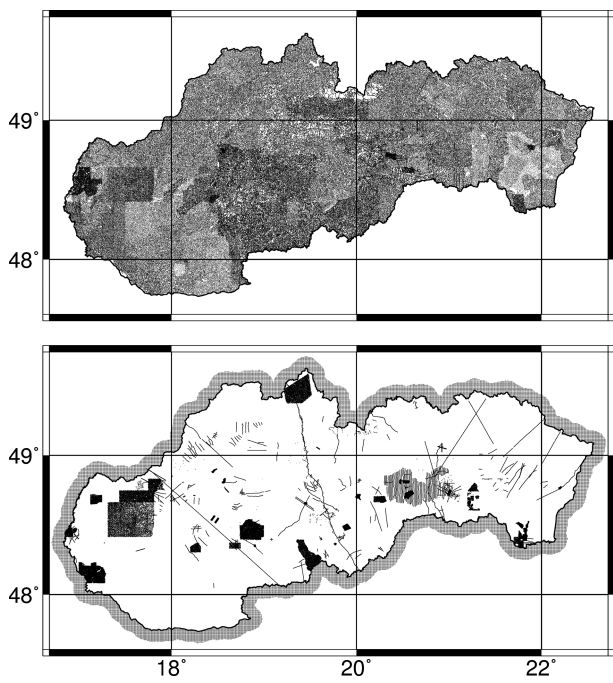


Figure 3. Spatial distribution of the input gravity stations. Upper panel, the GD1 data set; bottom panel, the GD2 (within the Slovak Republic) and GD3 (outside the Slovak Republic up to the spherical distance of 0.085°) data sets.

the Slovak Republic up to several kilometres from the borders are used.

(ii) *Global spherical harmonic models.* The long and medium wavelengths of the gravity field are modelled by EIGEN-6C4 up to its maximum harmonic degree 2190. It should be mentioned that due to Hotine–Jekeli's transformation applied in EGM2008, from which EIGEN-6C4 is partially derived, these models contain additional spherical harmonic coefficients in the spectral band of degrees 2160–2190 (see Pavlis *et al.* 2012). If using these models up to the maximum degree 2190, the series in eq. (2) should start at degree 2160 in order to avoid a spectral gap. We use the $\bar{C}_{2,0}$ coefficient of EIGEN-6C4 in the zero tide system. To transform the coefficient from the tide free system, in which the model is originally released, into the zero tide system, we used the relation adopted by the Calculation Service provided by the International Centre for Global Earth Models (ICGEM, <http://icgem.gfz-potsdam.de/ICGEM>),

$$\bar{C}_{2,0}^{\text{ZT}} = \bar{C}_{2,0}^{\text{TF}} + 0.3 (-1.39 \times 10^{-8}). \quad (11)$$

(iii) *Topographic models.* We approximate the topography by a national topographic model DMR-3.5 at the spatial resolution of 2 arcsec. The reference topography is represented by the spherical-harmonic-based model DTM2006.0, available up to degree 2190. For the same reason as in the previous paragraph, we truncate the spherical harmonic series of DTM2006.0 at degree 2159, which is the maximum degree of the ellipsoidal harmonic expansion in EGM2008 before applying Hotine–Jekeli's transformation.

For the validation purposes, we make use of four different gravity field quantities: the height anomaly derived from GNSS/levelling data, the gravity, the astrogeodetic deflection of the vertical and the vertical gravity gradient. These data types mutually complement each other and thus enable validation from different perspectives. For instance, the quasi-geoid signal is dominant mostly in low and medium frequencies, but it is rather insensitive to very short wavelengths. To be more specific, Rexer & Hirt (2015a) estimated that

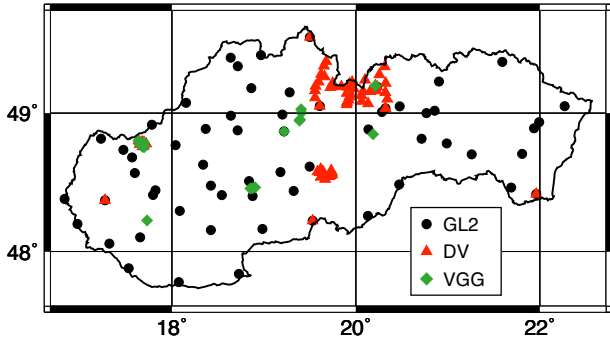


Figure 4. Spatial distribution of some of the test data sets. The positions of GL1 and GD4 are shown in Figs 9 and 10, respectively.

harmonic degrees from 10 801 to 90 000 contribute to the quasi-geoid at the level of ~ 0.13 cm in terms of degree variances which is about one order of magnitude smaller than the accuracy with which height anomalies can currently be derived (say ~ 1 cm). On the other hand, the gravity, the astrogeodetic deflection of the vertical and the vertical gravity gradient, all of which are related to the first- and second-order derivatives of the gravitational potential, are rich in this spectral band. In the case of gravity, for instance, Rexer & Hirt (2015a) estimated that the contribution of the same harmonic degrees as in the previous example is ~ 3.5 mGal in terms of degree variances. Since the magnitude of the gravity can be observed with an accuracy of about 0.01 mGal, that is, the signal-to-noise ratio is much more favourable than for height anomalies, ground gravity data can better assist in the evaluation of the high-frequency part of the signal than height anomalies. This clearly demonstrates the benefit of the combined validation. We use five data sets, some of which are shown in Fig. 4.

(i) *GNSS/levelling data.* The control GNSS/levelling points are divided into two sets, GL1 and GL2. The GL1 set consists of 347 control points with an accuracy of the height anomaly better than 2 cm. In the GL2 data set, 61 points of a slightly lower accuracy than in GL1 (~ 2 cm) are grouped together. For the sake of clarity, the GL1 points are not depicted in Fig. 4, but will be shown later.

(ii) *Independent gravity data.* 1264 gravity stations with an accuracy better than 0.02 mGal are used as a next data set GD4 (also shown later).

(iii) *Astrogeodetic deflections of the vertical.* This data set, hereafter denoted as DV, consists of 64 pairs of astrogeodetic deflections of the vertical with an expected accuracy of $\sim 0.2\text{--}0.3$ arcsec (Mojzeš *et al.* 2006). Note that this data set does not cover the whole territory. Instead, the observations are located mainly in the roughest part of the country (*cf.* Figs 1 and 4), and thus may provide a valuable information on the local quality of the solution.

(iv) *Terrestrial vertical gravity gradients.* Being the second-order derivative of the gravity potential, vertical gravity gradients possess a strong signal power in high frequencies and therefore may well serve for validating a high-resolution gravity field model. An approximation of the terrestrial vertical gravity gradient can be obtained as the difference in gravity per a sufficiently small vertical distance, say 1 m or so. In total, 20 terrestrial vertical gravity gradients observed following this scheme comprise the last data set VGG (Zahorec *et al.* 2014), see Fig. 4. Its accuracy is estimated to ~ 50 E ($1 \text{E} = 10^{-9} \text{ s}^{-2}$).

4 RESULTS

4.1 RTM assessment

In this section, we demonstrate the crucial role of the RTM-implied signal when forming residual gravity disturbances via eq. (5). The role of the terms $\gamma_r(\mathbf{r})$, $\delta g_r^{\text{SH}}(\mathbf{r})$ and $g_r^{\text{RTM}}(\mathbf{r})$ in this equation is to remove all the parts of the signal that can be modelled, thereby to smooth the gravity as much as possible. The smoothing step is of utmost importance in order to obtain a good least-squares fit, particularly in rugged terrain, where the gravity signal strongly varies.

In Fig. 5 (left panel), we show the residual gravity disturbances over the roughest part of the country. The corresponding statistics are reported in Table 1. Following Section 2.3, the RTM-implied signal is divided into two parts, the near- and far-zone effects. The near zone is defined by a spherical cap of the radius 0.08° centred at the computation point. This value is approximately equal to the spatial resolution of EIGEN-6C4. The far zone is the area beyond the inner zone up to the spherical distance of 0.5° from the computation point. This radius was found to be a good compromise between the accuracy and the computation time. A discussion on the choice of the radius in the context of degree-2159 spherical harmonic models can be found, for example, in Hirt (2010) or Hirt *et al.* (2010). At any rate, Table 1 shows the known fact that the near-zone effect plays a more important role than the far-zone's one (*cf.* the first three lines with the statistics in Table 1). This behaviour is inherent to the RTM method and stems from two facts. First, the kernel of Newton's integral decays when moving away from the computation point. Second, the residual terrain heights fluctuate around zero. As a consequence, with increasing distance, the contribution from residual terrain masses diminishes and cancels out to a large extent.

Next, we compare our RTMs with the freely available model ERTM2160 recently developed by Hirt *et al.* (2014). ERTM2160 provides four grids of the RTM-implied signal in terms of height anomalies, gravity disturbances and two components of deflections of the vertical, and it is designed to supplement spherical harmonic models like EGM2008 and EIGEN-6C4 with high-frequency signal. The residual terrain masses are modelled by rectangular prisms in the near zone and point-masses in the outer zone. The integration domain is 200 km from the computation point which is ~ 3.5 times larger than in our RTM computations. The topography within the inner zone is sampled at 7.2 arcsec resolution. The residual gravity disturbances obtained with ERTM2160 and their statistics are reported in Fig. 5 (right panel) and Table 1. Despite the larger integration domain in ERTM2160, noticeably smaller RMS values are obtained by the polyhedron-based modelling within the near zone. Since the mean values are close to zero, smaller RMS values indicate smoother residual gravity disturbances. It is, however, stressed that ERTM2160 is based on a coarser grid than our solution (7.2 versus 2 arcsec) and relies on different topographic models, which are also of great importance in the RTM method. Nevertheless, we believe that these results clearly point out the crucial role of RTM effects in the vicinity of observation points located in mountainous areas.

In the final computations, we obtain the near-zone effect on $g_r^{\text{RTM}}(\mathbf{r})$ via the polyhedron-based approach (up to 0.08°), while the contribution from the far zone (0.5°) is computed using the tesseroids.

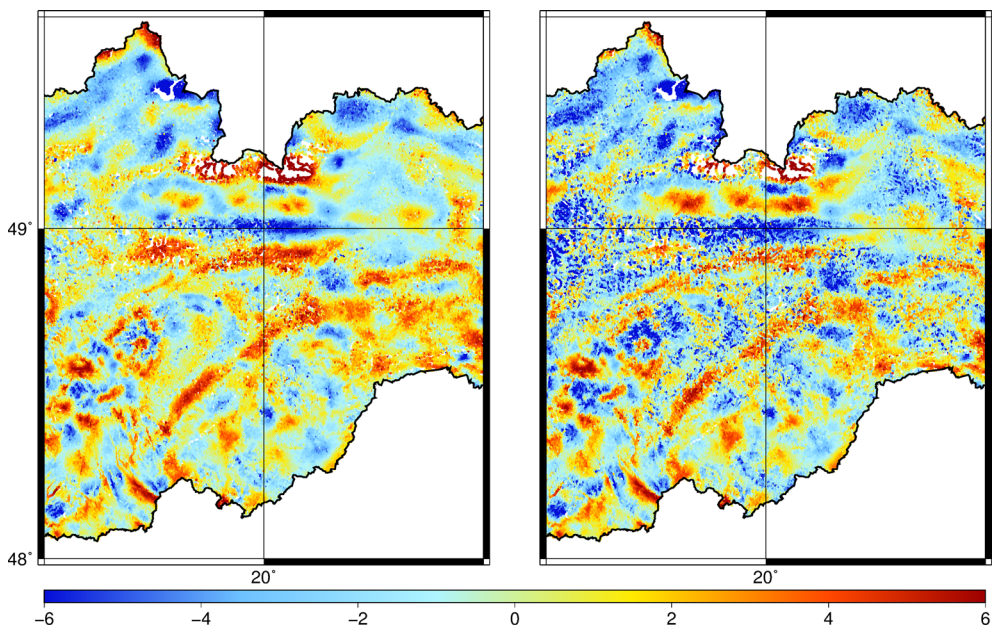


Figure 5. Residual gravity disturbances (in mGal) at 83 435 points (a part of the GD1 database) obtained after removing the contributions from the normal gravity field (GRS80, Moritz 2000), EIGEN-6C4 to degree 2190 and RTM data. The RTM component is computed in two ways: left panel, the near-zone effect is due to the polyhedron up to the spherical distance of 0.08° and the far-zone's one is due to the tesseroids up to 0.5°; right panel, bicubic interpolation from the ERTM2160 model. The statistics of the differences are shown in Table 1.

Table 1. Statistics of the residual gravity disturbances at 83 435 points (a part of the GD1 database) obtained using various RTM approaches. In the tesseroid-based approach, we performed a 10×10 horizontal subdivision of each tesseroid in the inner zone (see Grombein *et al.* 2013). Further subdivision did not improve the statistics significantly (below 0.001 mGal). The second line and the fourth line with the statistics are related to Fig. 5. The symbols ψ_i and ψ_o denote spherical distances defining the inner and outer zone, respectively.

Inner zone	Outer zone	min (mGal)	max (mGal)	mean (mGal)	RMS (mGal)
Tesseroids ($\psi_i = 0.08^\circ$)	Tesseroids ($\psi_o = 0.5^\circ$)	-18.926	25.758	-0.221	3.062
Polyhedron ($\psi_i = 0.08^\circ$)	Tesseroids ($\psi_o = 0.5^\circ$)	-18.903	24.541	-0.108	2.367
Polyhedron ($\psi_i = 0.08^\circ$)	Tesseroids ($\psi_o = 1^\circ$)	-18.894	24.552	-0.102	2.367
ERTM2160 (Hirt <i>et al.</i> 2014)		-19.451	22.559	-0.717	2.854

Table 2. Statistics of the residual gravity disturbances entering the least-squares adjustment. Note that the mean values for the GD2 and GD3 databases are significantly different from zero which is a consequence of the rather irregular spatial distribution of the gravity stations (see the bottom panel in Fig. 3).

Data set	Number of points	min (mGal)	max (mGal)	mean (mGal)	RMS (mGal)
GD1	211 631	-20.230	24.541	0.102	2.573
GD2	107 416	-28.445	23.668	0.619	3.097
GD3	32 199	-30.536	41.727	2.780	6.821

4.2 Regional gravity field solutions

We use a total of 351 246 gravity stations to derive the residual component of the gravity field; see Table 2 for the statistics. To reduce edge effects, the data from the GD3 database are taken up to the spherical distance of 0.085° from the borders which is slightly more than the spatial resolution of degree-2159 spherical harmonic models. Since we expect different quality of the input gravity databases, each one is treated as a separate observation group with its own variance factor to be determined by the variance component estimation approach. The spatial distribution of the input data enables to expand the residual gravity field up to degree $n_{\max} = 21\,600$

corresponding to 30 arcsec spatial resolution. In some parts of the territory, the maximum degree could be even higher, for example, 32 400 (20 arcsec), which would result in a model with varying spatial resolution. This option, however, is not studied here. Instead, we use the single value $n_{\max} = 21\,600$. The spatial distribution of the points $\mathbf{r}_i \in \Omega_R$ is defined by the Reuter grid with the parameter α being equal to $n_{\max} + 1$. Of this grid, only the points up to the spherical distance of 0.125° from the borders are used. Note that the points \mathbf{r}_i slightly exceed the data area in order to improve the least-squares fit. The value 0.125° was found empirically. The total number of the points \mathbf{r}_i , and thus also of the expansion coefficients, is 77 769, that is, there is ~ 4.5 times more observations than the unknowns. EIGEN-6C4 up to its maximum degree 2190 is used to model the long and medium wavelengths of the gravity field.

Considering that we model the residual gravity field up to degree as high as 21 600, the total number of expansion coefficients 77 769 is extremely small, and demonstrates one of the key benefits of the combined approach (SRBFs plus spherical harmonics). In this case, regional gravity field modelling to degree 21 600 via the combined approach requires only ~ 4.9 millions of coefficients (the number of coefficients in EIGEN-6C4 plus the number of expansion coefficients), while more than 466 millions of coefficients would be needed in global spherical-harmonic-based approaches. Naturally,

Table 3. Statistics of the least-squares residuals using $n_{\min} = 0$ and $n_{\min} = 2160$ in eq. (2). The last column shows the percentage of the residuals falling into the mGal-level.

Data set	min (mGal)	max (mGal)	mean (mGal)	RMS (mGal)	-1 to 1 mGal (per cent)
Solution with $n_{\min} = 0$					
GD1	-14.191	19.900	-0.056	0.666	90
GD2	-25.476	27.530	-0.026	0.709	92
GD3	-27.639	27.191	-1.308	3.699	34
Solution with $n_{\min} = 2160$					
GD1	-18.108	20.313	-0.087	1.374	64
GD2	-25.691	26.785	-0.197	0.930	82
GD3	-45.068	31.733	-2.662	6.770	17

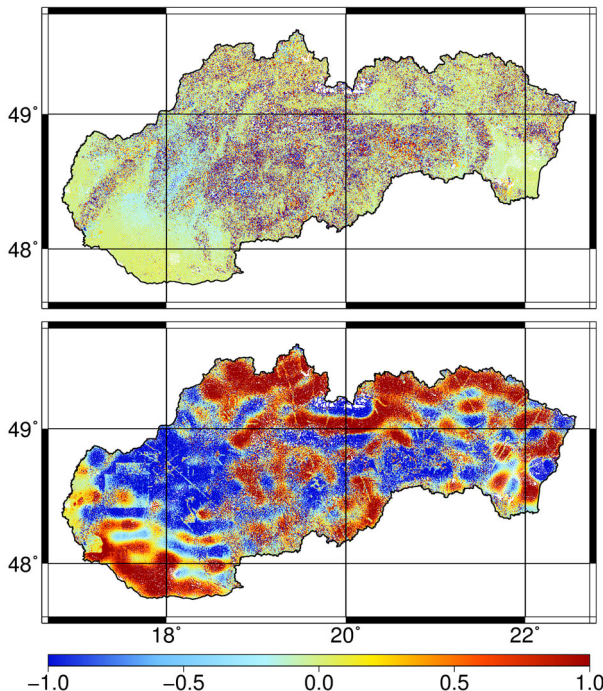


Figure 6. Least-squares residuals (mGal) related to the GD1 database using $n_{\min} = 0$ (upper panel) and $n_{\min} = 2160$ (bottom panel). See Table 3 for the statistics.

the total number of coefficients involved in the combined approach increases with the size of the recovery area, but in regional applications, a substantial reduction can essentially always be expected. This benefit is rather insignificant in satellite applications where the value of n_{\max} usually does not exceed degree 250 or so. On the other hand, the limitations of the combined approach should be kept in mind (see Section 1). At any rate, on the regional scale, band-limited SRBFs, particularly Shannon's one, in combination with high-degree spherical harmonic models seem to be a good alternative to global ultra-high-degree spherical harmonic modelling as performed, for example, in Rexer & Hirt (2015b); see also the discussion in Section 1 of this paper.

In Table 3, we show the statistics of the least-squares residuals using $n_{\min} = 0$ and $n_{\min} = 2160$ in the series expansion of SRBFs (see eq. 2). The residuals related to the GD1 database are depicted in Fig. 6. Though the signal from EIGEN-6C4 was removed from the input gravity data, the least-squares residuals for $n_{\min} = 2160$

clearly imply that the harmonic degrees below 2160 are still present in the input residual gravity disturbances.

To examine this issue, we performed a spectral decomposition (see e.g. Freed & Schneider 1998) of the residual gravity disturbances in spherical approximation (the negative first-order radial derivative of the residual potential) synthesized from the estimated expansion coefficients ($n_{\min} = 0$), see Fig. 7. We decomposed the signal into six spectral bands: three bands to degree 2159 (0–539, 540–1079, 1080–2159) and three bands beyond that degree (2160–5399, 5400–10 799 and 10 800–21 600). The residual signal below degree 2160 originates mainly from inaccuracies in the input gravity data, EIGEN-6C4 and the RTM-implied signal. In Section 4.3, each evaluation using independent data leads to a conclusion that the most dominant part of this signal seems to be due to the errors in EIGEN-6C4 and the RTM, while the errors of the input gravity data are expected to play a minor role, mostly of a high-frequency nature. This implies that, in this particular case, the series expansion in eq. (2) should start at a lower degree than 2160 in order to absorb this useful part of the signal. This step, in turn, results in a better solution as will be shown in Section 4.3. Instead of deciding which value of n_{\min} should be used, we simply put $n_{\min} = 0$, though it is clear that harmonic degrees below, say, 180 cannot be properly retrieved from such a small area.

As for the upper part of the spectrum ($n > 2159$) in Fig. 7, note that the signal depicted does not represent (an approximation of) the true gravity signal, because of the removed short-scale contribution implied by the RTM. As expected, the largest variations of the residual gravity disturbances are in mountainous areas (cf. Fig. 1), reaching the minimum and maximum values of about -23 mGal and 49 mGal, respectively.

The standard deviations obtained by the variance component estimation approach read (the solution with $n_{\min} = 0$) $\hat{\sigma}_1 = 0.74$ mGal, $\hat{\sigma}_2 = 0.73$ mGal and $\hat{\sigma}_3 = 4.0$ mGal. These estimates confirm that, as expected, the quality of the GD3 database is significantly lower when compared with GD1 and GD2 (see Section 3). The close standard deviations for the GD1 and GD2 databases imply that these data sets could be merged together prior to the least-squares adjustment and treated as a single observation group. Note, however, that the obtained standard deviations represent the quality of the fit rather than the actual accuracy of the gravity databases.

Despite the large effort we put into the RTM computations, the residuals in Fig. 6 clearly imply a correlation with the topography (cf. Figs 6 and 1). We believe that RTM effects should be the key candidate for further improvements of our combined regional gravity field model. However, rather than by improving the RTM technique itself (polyhedral modelling offers a high-quality computation of local terrain effects; see e.g. Tsoulis 2003), we expect that significantly larger progress can be achieved by using a DTM of a higher spatial resolution and quality (not available to us at this time).

4.2.1 Corrections to the spherical harmonic coefficients of degree-2159 harmonic models

In the previous section, we came to a conclusion that the residual signal below degree 2160 (see Fig. 7), hereafter called the correction signal, is mostly due to the errors in both EIGEN-6C4 and the RTM. Therefore, we attempted to separate these two error sources by computing the same solution as in the previous section ($n_{\min} = 0$), but completely without using the RTM technique, that is, the term g_r^{RTM} in eq. (5) is omitted. Naturally, this solution is of significantly lower quality in high frequencies ($n > 2159$), but we expect that it might

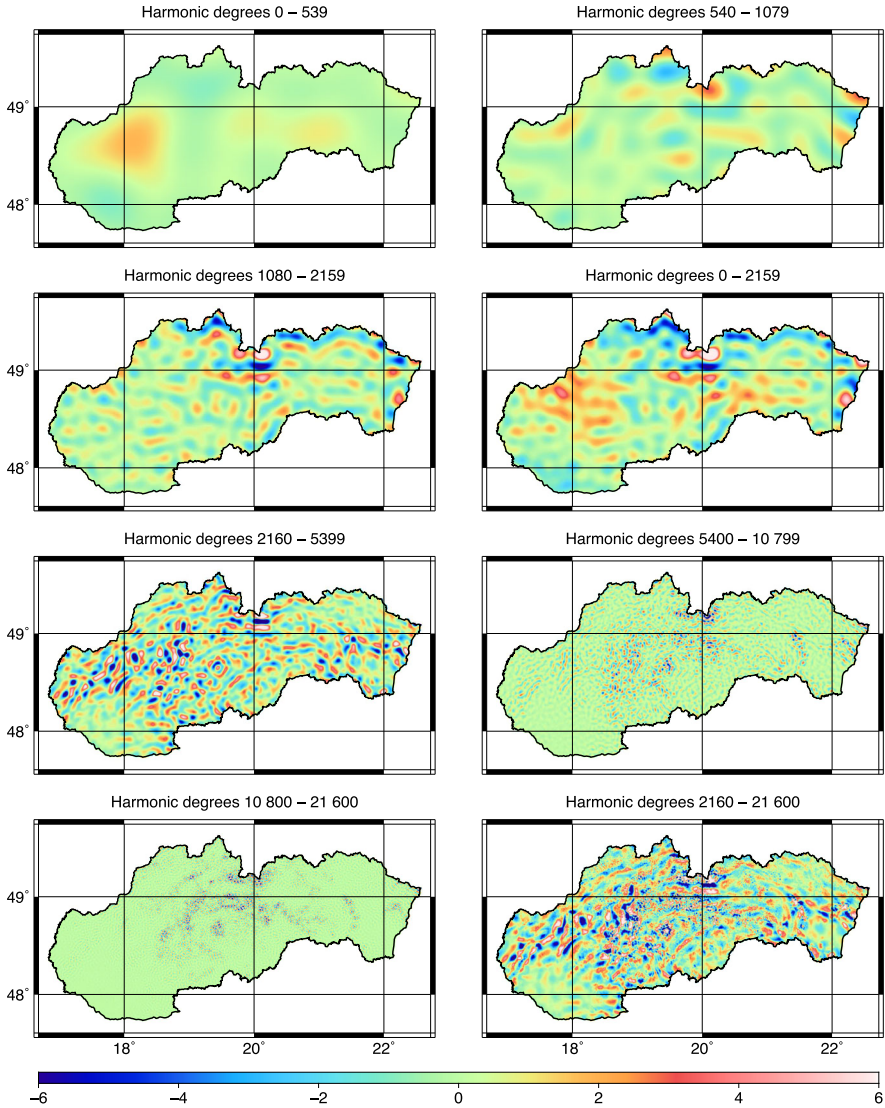


Figure 7. Spectral decomposition of residual gravity disturbances in spherical approximation (mGal) synthesized from the expansion coefficients estimated with $n_{\min} = 0$ in eq. (2).

partially enable to identify the EIGEN-6C4-related errors in the input residual gravity disturbances. The correction signal derived from the solution free of the RTM technique is shown in Fig. 8. We observe a somewhat different character of the correction signal when compared with the same spectral band in Fig. 7 (see the right panel in Fig. 8). This implies that despite removing harmonic degrees below 2160 from the DTM, the RTM might propagate some long- and medium-wavelength features into the combined model which might be related to the approximation errors mentioned in Section 2.3. Further study is, however, necessary to examine this issue.

For many practical applications relying on EIGEN-6C4, it would be beneficial to have the correction signal at our disposal in such a form that it could easily be used to improve gravity field quantities computed from EIGEN-6C4 within this region. Fortunately, there is a simple, yet exact, way of how to achieve this. Since our goal is to derive the correction signal related to EIGEN-6C4 and the RTM clearly affects it, we deal in the following only with the solution free of the RTM technique.

When deriving the SRBF-based part of the regional model, we neglect all the expansion coefficients referring to the nodal points

$\mathbf{r}_i \in \Omega_R$ located outside the area of interest. By doing this, we implicitly put $a_i = 0$ for all \mathbf{r}_i beyond this area. This means that if we merge the zero as well as the non-zero expansion coefficients, the signal from these coefficients will be defined over the whole sphere Ω_R , and it can also be harmonically upward/downward continued as usually. In practice, of course, it is not necessary to work with the zero coefficients, as they automatically vanish in the synthesis step (see eq. 1); this is just for the sake of clarity. It is also obvious that, beyond the borders, the signal will not represent the correction signal as understood in the previous paragraph. However, after the signal is ‘extended’ over the whole sphere, it can be converted into a set of spherical harmonic coefficients, for example, by means of numerical quadratures. For instance, the transformation by Driscoll & Healy (1994) is *exact*, provided that the signal to be converted is band-limited, which holds true for the correction signal, and sampled at a specific grid prescribed by the quadrature. The latter can be fulfilled in the manner described above. Further exact quadratures can be found, for example, in Sneeew (1994). However, if taking advantage of the relation between band-limited SRBFs and spherical harmonics, the whole inversion procedure can be performed in a

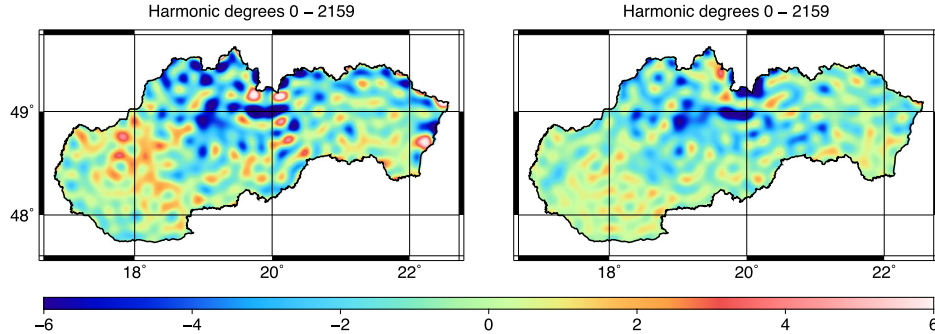


Figure 8. Left panel: residual gravity disturbances in spherical approximation (mGal) synthesized from the expansion coefficients estimated without using the RTM technique ($n_{\min} = 0$). Right panel: difference with respect to the solution with the RTM technique included (the right panel in the second row of Fig. 7). Used is the same colour bar as in Fig. 7.

Table 4. Statistics of the differences between the predicted and GNSS/levelling-based height anomalies. The values are shown *before / after* the removal of the constant bias term. The correction coefficients are related to the solution derived without using the RTM data.

Variant	min (m)	max (m)	mean (m)	RMS (m)
The GL1 data set (347 points)				
EIGEN-6C4	-0.687 / -0.164	-0.424 / 0.099	-0.523 / 0.000	0.525 / 0.036
EIGEN-6C4 + Correction coefficients	-0.741 / -0.199	-0.432 / 0.110	-0.542 / 0.000	0.543 / 0.037
EIGEN-6C4 + RTM	-0.656 / -0.114	-0.436 / 0.106	-0.542 / 0.000	0.543 / 0.031
EIGEN-6C4 + RTM + the Shannon SRBF ($n_{\min} = 0$)	-0.648 / -0.112	-0.420 / 0.115	-0.536 / 0.000	0.537 / 0.027
EIGEN-6C4 + RTM + the Shannon SRBF ($n_{\min} = 2160$)	-0.653 / -0.111	-0.435 / 0.107	-0.542 / 0.000	0.543 / 0.030
The GL2 data set (61 points)				
EIGEN-6C4	-0.650 / -0.098	-0.410 / 0.141	-0.552 / 0.000	0.553 / 0.036
EIGEN-6C4 + Correction coefficients	-0.685 / -0.109	-0.436 / 0.140	-0.576 / 0.000	0.578 / 0.045
EIGEN-6C4 + RTM	-0.653 / -0.094	-0.463 / 0.096	-0.559 / 0.000	0.560 / 0.034
EIGEN-6C4 + RTM + the Shannon SRBF ($n_{\min} = 0$)	-0.659 / -0.110	-0.463 / 0.087	-0.550 / 0.000	0.551 / 0.035
EIGEN-6C4 + RTM + the Shannon SRBF ($n_{\min} = 2160$)	-0.652 / -0.094	-0.464 / 0.094	-0.558 / 0.000	0.559 / 0.034

more efficient way. Again, without any approximations, expansion coefficients related to band-limited SRBFs can be transformed into spherical harmonic coefficients c_{nm} via (Eicker 2008)

$$c_{nm} = \frac{1}{4\pi R^2} \frac{R_{\text{SH}}}{GM_{\text{SH}}} \phi_n \left(\frac{R}{R_{\text{SH}}} \right)^{n+1} \sum_{i=1}^I a_i \bar{Y}_{nm} \left(\frac{\mathbf{r}_i}{R} \right), \quad (12)$$

where GM_{SH} and R_{SH} are, respectively, the geocentric gravitational constant and the radius of the reference sphere to which the coefficients c_{nm} are to be scaled. The symbol \bar{Y}_{nm} denotes the 4π fully normalized surface spherical harmonic function of degree n and order $m = -n, \dots, n$. Unlike the numerical quadratures, eq. (12) avoids the direct SRBF synthesis at the grid points which results in a much faster transformation, especially when increasing the maximum degree of the expansion. We therefore prefer eq. (12) in combination with the algorithm by Fukushima (2012) to obtain \bar{Y}_{nm} for high degrees and orders.

In this way, we transformed the correction signal derived from the solution free of the RTM technique into a set of spherical harmonic coefficients, which can be added to EIGEN-6C4 obtaining some kind of its improved version. Though EIGEN-6C4 originally describes the gravity field globally, the use of the new model is restricted to the area of interest, in this case the Slovak Republic. This is because the extension of the correction signal deteriorates the model beyond this area. Furthermore, gravity field quantities should only be synthesized at the topography (or in its close vicinity). The primary exploitation of the new model is therefore in gravity-field-related terrestrial applications within this region.

We note that the correction signal was derived via the Shannon SRBF, which ensures that the signal power will not be damped by the SRBF itself, see eq. (12) and Section 2.1. The improvement of EIGEN-6C4 due to the correction coefficients is demonstrated in the following section.

4.3 Evaluation of the regional gravity field models using independent data

4.3.1 GNSS/levelling data

We compute height anomalies from the combined model via Bruns's formula. The disturbing potential in this equation is obtained as the sum of: (i) the disturbing potential from EIGEN-6C4 to degree 2190, (ii) the gravitational potential from the RTM and (iii) the residual gravitational potential synthesized from the expansion coefficients. The statistics of the differences between the height anomalies derived from the combined model and from the GNSS/levelling data are reported in Table 4. It can be seen that the RTM data and the SRBF-based part of the model improve the height anomalies at the GL1 points by 25 per cent. In the case of the GL2 data set, the gain in accuracy is on a negligible level if taking into account the accuracy of this data set (~ 2 cm). At the GL1 data, the correction coefficients decrease insignificantly the quality of height anomalies from EIGEN-6C4, but we observe a noticeable deterioration at the GL2 data set. No satisfactory explanation for the latter behaviour has yet been found and the GL2 database remains the only one

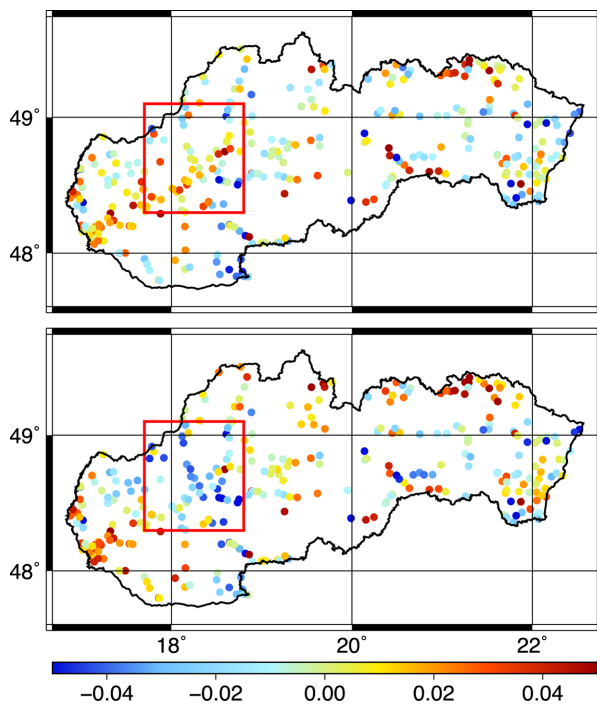


Figure 9. Differences (m) between the predicted and GNSS/levelling-based height anomalies at the GL1 data set. Upper panel, solution with $n_{\min} = 0$; bottom panel, solution with $n_{\min} = 2160$. The statistics are reported in Table 4. The red lines bound the area where the residual signal below degree 2160 clearly improves the solution (see also the same area in Fig. 7 in the spectral band of degrees 0–539).

for which we observe inferior results after adding the correction coefficients to EIGEN-6C4.

The GL2 data set has been used several times to validate quasi-geoid solutions within this territory. We therefore provide a brief overview of some recent studies by reporting the standard deviations achieved by other scientific groups. Each of the following solutions is free of the fitting technique. Čunderlík *et al.* (2008) achieved an accuracy of 17.1 cm using the boundary element method, Šprlák (2008) reached 3.4 cm via an FFT-based method, Fašková *et al.* (2010) reported 7.8 cm using the finite element method and, finally, Macák *et al.* (2014) achieved the standard deviation of 5.9 cm using the finite volume method with the oblique derivative boundary condition.

The large number of control points in the GL1 data set provides a good opportunity to identify whether our solutions (or the GNSS/levelling data) suffer from systematic deformations. In Fig. 9, we show the differences achieved with our two combined models. It can be seen that some of the long-wavelength features in the solution with $n_{\min} = 2160$ are slightly reduced when using $n_{\min} = 0$. Not shown here, but our solution with $n_{\min} = 0$ shows the smallest systematic deformations when compared with the quasi-geoids developed by the aforementioned scientific groups. The quasi-geoid by Šprlák (2008), who reached essentially the same accuracy at the GL2 data set as we reported in Table 4, shows similar long-wavelength discrepancies at the GL1 points as in the bottom panel of Fig. 9 but with a slightly larger amplitude. Based on this comparison and on the results in Table 4, we expect that our solution with $n_{\min} = 0$ provides the most accurate quasi-geoid developed so far over this territory. It should also be noted that the accuracy we achieved approaches the accuracy of the control height anomalies themselves.

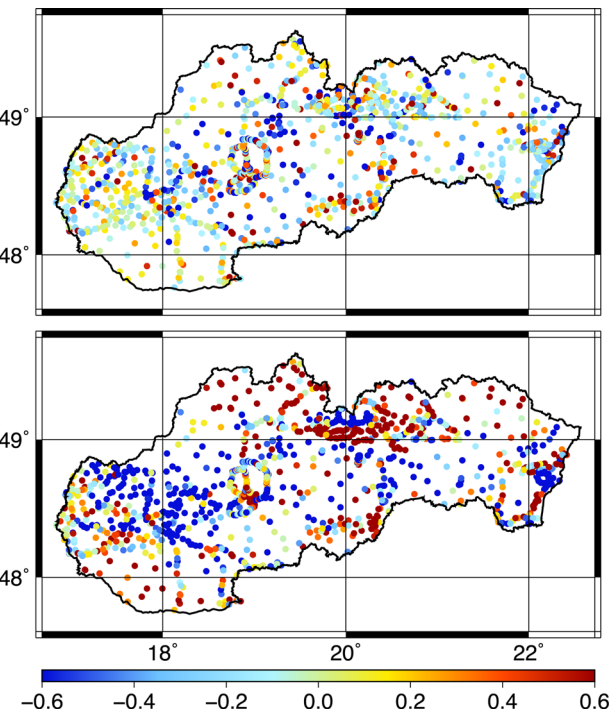


Figure 10. Differences (mGal) between the predicted and independent gravity data at the GD4 database. Upper panel, solution with $n_{\min} = 0$; bottom panel, solution with $n_{\min} = 2160$. The statistics are reported in Table 5.

4.3.2 Independent gravity data

The gravity data in the GD4 database offer further insight into the performance of our models. This evaluation is valuable mostly because of the following reasons. (i) Gravity, as the magnitude of the gravity vector, is in a functional relation with the first-order derivatives of the gravity potential, hence its signal power in high frequencies is stronger than that of height anomalies, see Section 3. This is especially useful to validate the short-scale properties of our combined models. (ii) The gravity data in the GD4 database are of high accuracy (better than 0.02 mGal) and thus may serve as a high-quality benchmark for the evaluation. (iii) The data in GD4 are densely distributed over the whole territory (see Fig. 10).

We obtain the predicted gravity as the magnitude of the gravity vector, which is computed as the sum of (i) the gravity vector synthesized from EIGEN-6C4 to degree 2190, (ii) the gravitational vector from the RTM and (iii) the residual gravitational vector computed from the estimated expansion coefficients. Finally, the atmospheric effect (see Section 2.2) is removed in order to obtain values that can directly be compared with terrestrial gravity observations.

The statistics of the differences are reported in Table 5. We observe that the RTM-implied gravity signal improves the gravity from EIGEN-6C4 by ~ 83 per cent in terms of the RMS error. After further adding the SRBF-based part of the signal ($n_{\min} = 0$), the improvement rate is of about 97 per cent. Clearly, the solution with $n_{\min} = 2160$ is inferior to the one with $n_{\min} = 0$ which can also be seen from Fig. 10. Note that the character of the discrepancies shown in the bottom panel of Fig. 10 is very similar, but of opposite sign, to that of the correction signal (harmonic degrees 0–2159 in Fig. 7). Since the GD4 database is composed of high-quality terrestrial gravity data and is completely independent from the GD1, GD2 and GD3 databases, this provides a strong evidence that, as claimed in Section 4.2, this signal is due to the inaccuracies in EIGEN-6C4

Table 5. Statistics of the differences between the predicted and independent gravity data. The correction coefficients are related to the solution derived without using the RTM data.

Variant	min (mGal)	max (mGal)	mean (mGal)	RMS (mGal)
The GD4 data set (1264 observations)				
EIGEN-6C4	-61.851	80.078	6.815	17.091
EIGEN-6C4 + Correction coefficients	-59.801	71.752	6.071	16.221
EIGEN-6C4 + RTM	-13.715	8.376	-0.379	2.862
EIGEN-6C4 + RTM + the Shannon SRBF ($n_{\min} = 0$)	-3.578	3.945	-0.090	0.526
EIGEN-6C4 + RTM + the Shannon SRBF ($n_{\min} = 2160$)	-8.192	7.393	-0.223	1.359

Table 6. Statistics of the differences between the predicted and observed deflections of the vertical. The values are reported in the form: *the meridional (ξ) / the prime vertical (η) component*. The correction coefficients are related to the solution derived without using the RTM data.

Variant	min (arcsec)	max (arcsec)	mean (arcsec)	RMS (arcsec)
The DV data set (64 pairs of ξ/η)				
EIGEN-6C4	-3.568 / -7.815	6.316 / 3.769	-0.127 / 0.415	2.184 / 1.966
EIGEN-6C4 + Correction coefficients	-3.331 / -7.637	6.381 / 3.810	-0.162 / 0.300	2.157 / 1.899
EIGEN-6C4 + RTM	-1.688 / -1.203	2.440 / 1.617	-0.134 / 0.247	0.712 / 0.627
EIGEN-6C4 + RTM + the Shannon SRBF ($n_{\min} = 0$)	-1.015 / -0.673	0.922 / 1.159	-0.036 / 0.111	0.366 / 0.419
EIGEN-6C4 + RTM + the Shannon SRBF ($n_{\min} = 2160$)	-1.597 / -1.039	1.603 / 1.490	-0.103 / 0.215	0.583 / 0.561

and in the RTM, and it does not originate from the input gravity data in GD1 or GD2.

Finally, Table 5 reveals that adding the correction coefficients to the EIGEN-6C4 model reduces the RMS error by ~ 5 per cent. Given that gravity is a highly spatially varying quantity, and thus a significant enhancement cannot be expected in such a rather rough region when using a series expansion to degree 2159, this improvement rate is definitely not negligible.

4.3.3 Deflections of the vertical

To obtain astrogeodetic deflections of the vertical from the combined model, we first compute the gravity disturbance vector from EIGEN-6C4, RTM data and from the expansion coefficients, similarly as in the previous section. For the simplicity, this step is performed in the LNOF^s, but after the computations, the resulting gravity disturbance vector is rotated into the LNOF^e. Then, the horizontal components of the vector are divided by the magnitude of the normal gravity vector and the effect of the curvature of the normal plumb line is added to the meridional component of the vertical deflection (see e.g. Jekeli 1999). The permanent tide effect is not treated separately as in Jekeli (1999), since it is accounted for in the $\bar{C}_{2,0}^{ZT}$ coefficient (see Section 3).

The statistics of the differences between the synthesized and observed vertical deflections are shown in Table 6. After adding the RTM effect and the SRBF-based part of the model, we achieved an improvement rate of ~ 80 per cent. Similarly as in the previous section, the solution with $n_{\min} = 0$ outperforms the one with $n_{\min} = 2160$, and the correction coefficients improve the EIGEN-6C4 model. The latter enhancement is, however, negligible. It has to be noted that, similarly as in the case of height anomalies, the RMS error of the differences ($n_{\min} = 0$) approaches the expected accuracy of the observations (~ 0.2 –0.3 arcsec).

4.3.4 Vertical gravity gradients

Many studies deal with the combination of spherical harmonic models and the RTM technique in terms of frequently used gravity field

quantities like height anomalies, gravity anomalies/disturbances or vertical deflections. In recent years, RTM applications related to the second-order derivatives of the gravitational potential have also began to emerge, mainly due to the GOCE satellite. Typically, these studies are restricted to computation points located at the orbit of the GOCE satellite, that is, ~ 250 km above the Earth's surface. It seems, however, that RTM applications coping with the computation of the tensor near the Earth's surface are only little discussed in the literature (e.g. Kadlec 2011). In this section, we report our experience and show some results of modelling the gravity tensor, particularly the vertical gravity gradient, near the Earth's surface using spherical harmonics, the RTM technique, SRBFs and their combinations.

When computing the gravity tensor, we again work in the LNOF^s at first. The gravity tensor is computed as the sum of: (i) the gravity tensor synthesized from EIGEN-6C4 to degree 2190, (ii) the gravitational tensor derived from the RTM and (iii) the residual gravitational tensor from the expansion coefficients. In Appendix, we provide a numerically stable form of the second-order derivatives of SRBFs in the LNOF^s. Finally, the synthesized gravity tensor is rotated from LNOF^s into LNOF^e. The ZZ-component of the rotated tensor is here understood as the vertical gravity gradient. Regarding the accuracy of the synthesized and observed vertical gravity gradients, the rotation can be omitted, as its effect is about one order of magnitude smaller than the accuracy of our observations (~ 50 E).

The statistics of the differences between the synthesized and observed vertical gravity gradients are reported in Table 7. It can be seen that the RMS error dropped by about 70 per cent after adding the RTM contribution, but only a negligible improvement is achieved when further including the SRBF-based part of the combined model. This is not surprising given that the vertical gravity gradient is a highly terrain-sensitive quantity. In our case, the most dominant portion of the short-scale signal is covered by the RTM, derived using a high-resolution DTM (2 arcsec), while the SRBF-based part of the model, expanded up to degree 21 600, describes the residual signal at a $15 \times$ lower spatial resolution (30 arcsec). This leads to a conclusion that we might even neglect the SRBF-based part of the model and an effort should be put into the RTM

Table 7. Statistics of the differences between the predicted and observed vertical gravity gradients. The correction coefficients are related to the solution derived without using the RTM data.

Variant	min (E)	max (E)	mean (E)	RMS (E)
The VGG data set (20 observations)				
EIGEN-6C4	-2619.7	1239.3	-297.2	913.7
EIGEN-6C4 + Correction coefficients	-2617.4	1229.3	-298.6	912.6
EIGEN-6C4 + RTM	-775.9	322.4	-151.3	280.3
EIGEN-6C4 + RTM + the Shannon SRBF ($n_{\min} = 0$)	-766.7	315.5	-152.6	279.3
EIGEN-6C4 + RTM + the Shannon SRBF ($n_{\min} = 2160$)	-770.9	319.1	-157.7	280.8

technique in order to achieve further enhancement. Finally, we mention that the solution with $n_{\min} = 2160$ is again of lower quality, and that the corrections coefficients change the EIGEN-6C4 model insignificantly in terms of vertical gravity gradients.

Our last remark on vertical gravity gradient modelling concerns the RTM computations. It is known that the tesseroid-based approach cannot be applied to the tensor computations at the vicinity of tesseroids due to the strong singularities of the integral kernels (Grombein *et al.* 2013). In our computations, we used tesseroids to approximate the residual terrain masses located within the outer zone (from the spherical distance of 0.08° up to 0.5°). The question that arises is whether the spherical distance of 0.08° is sufficiently large to avoid the singularity-related issues. We therefore repeated the RTM computations, but using the polyhedron-based approach in the whole integration domain including the outer zone. We note that the polyhedron-based approach we used is free of these singularities and thus may serve as a benchmark. We obtained a very good agreement between both RTMs which implies that the proposed approach can be applied even to terrestrial applications. The statistics of the differences between the two RTMs in terms of the vertical gravity gradient are: min = -0.015 E, max = 0.010 E, mean = -0.001 E, RMS = 0.006 E. Note that the estimated accuracy of the observed vertical gravity gradients is ~ 50 E.

5 SUMMARY AND DISCUSSION

We have discussed and applied an approach to regionally improve the currently available high-degree spherical harmonic models like GECO, EIGEN-6C4 and EGM2008. In the strategy presented, we model the gravity field via a combination of spherical harmonics, band-limited SRBFs and the RTM method. The high-frequency gravity signal (beyond degree-2159 harmonic models) is derived mainly from dense terrestrial gravity data and is expanded in terms of SRBFs up to degree 21 600, which corresponds to 30 arcsec spatial resolution. The ultra-short wavelengths beyond this scale rely purely on RTM data computed under the constant mass-density assumption using a topographic model at 2 arcsec spatial resolution. While the RTM data can separately be used to improve degree-2159 harmonic models, the SRBF-based part of the model should always be treated in connection with the RTM data. One should, however, keep in mind that, in general, the resulting signal cannot be geophysically interpreted beyond the 30 arcsec resolution, as this short-scale information comes solely from the RTM model.

A thorough evaluation of the combined model has revealed a significant gain in accuracy when compared with degree-2159 harmonic models, in our case EIGEN-6C4, depending on the gravity field quantity. The largest improvement rate was observed for gravity, 97 per cent, while the enhancement in height anomalies, 25 per cent, is smaller, but crucial to provide a high-quality quasi-geoid model. In addition to the combined model itself, we have

also estimated a correction signal to EIGEN-6C4, and shown that it improves gravity, vertical deflections and vertical gravity gradients synthesized from this model over our study area. For some reason unknown to us, we found a noticeable deterioration at one GNSS/levelling data set (GL2) after adding the correction coefficients. The correction signal is provided as a set of spherical harmonic coefficients corresponding to the EIGEN-6C4 model to which it can be added.

Apart from the terrestrial gravity data, the key feature to deliver a high-quality model in mountainous areas is the quality of the RTM-implied signal. We have shown that the use of a polyhedron-based approach in the inner zone should be preferred over the tesseroid-based one, particularly in rough regions. The residual terrain modelling of terrestrial vertical gravity gradients has been shown to be feasible, though, not surprisingly, it seems that this requires extremely detailed knowledge of the innermost topography, say at a spatial resolution of a few metres. Nevertheless, using an RTM derived from a topographic model at 2 arcsec spatial resolution, we were able to reduce the RMS error of the EIGEN-6C4-based vertical gravity gradients by ~ 70 per cent.

Undoubtedly, one of the main benefits of the combined approach when working with high-resolution regional data is the substantial reduction of the expansion coefficients to be determined. Various data sets, for instance terrestrial gravity data or DTMs, are available at a very high spatial resolution, but are frequently spatially restricted to a relatively small part of the Earth's surface. This makes the use of global modelling techniques based solely on spherical harmonics inefficient, if not entirely impossible. The combined approach applied in this study can therefore be viewed from a more general perspective. In combination with spherical harmonics, the Shannon SRBF—thanks to its capability of the orthogonal decomposition (see e.g. Freedon & Schneider 1998)—offers an efficient tool to handle also other gravity-field-related tasks on the regional scale. It might be helpful, for instance, when modelling the gravitational potential generated by topographic masses represented by a high-resolution band-limited surface (see Hirt & Kuhn 2014).

ACKNOWLEDGEMENTS

BB and JJ were supported by the projects APVV-0072-11 and VEGA 1/0954/15. JP was supported by APVV-0194-10 and VEGA 1/0714/15. AB was supported by the projects GA13-36843S and RVO: 67985815. We thank the Geodetic and Cartographic Institute Bratislava for providing the DTM DMR-3.5, GNSS/levelling data (GL1 and GL2) and the GD4 gravity data set. The computations were performed at the HPC centre at the Slovak University of Technology in Bratislava, which is a part of the Slovak Infrastructure of High Performance Computing (SIVVP project, ITMS code 26230120002, funded by the European region development funds, ERDF). Valuable comments by two anonymous reviewers

are gratefully acknowledged. We thank ICGEM for the access to the global gravity field models. The maps were produced using the Generic Mapping Tools (Wessel & Smith 1998).

REFERENCES

- Balmino, G., Vales, N., Bonvalot, S. & Briais, A., 2012. Spherical harmonic modelling to ultra-high degree of Bouguer and isostatic anomalies, *J. Geod.*, **86**, 499–520.
- Bentel, K., Schmidt, M. & Denby, C.R., 2013a. Artifacts in regional gravity representations with spherical radial basis functions, *J. Geodetic Sci.*, **3**, 173–187.
- Bentel, K., Schmidt, M. & Gerlach, C., 2013b. Different radial basis functions and their applicability for regional gravity field representation on the sphere, *Int. J. Geomath.*, **4**, 67–96.
- Blais, J.A.R., Provins, D.A. & Soofi, M.A., 2006. Spherical harmonic transforms for discrete multiresolution applications, *J. Supercomput.*, **38**, 173–187.
- Bucha, B., Bezd  k, A., Sebera, J. & Jan  k, J., 2015. Global and regional gravity field determination from GOCE kinematic orbit by means of spherical radial basis functions, *Surv. Geophys.*, **36**, 773–801.
- Claessens, S.J., Featherstone, W.E. & Barthelmes, F., 2001. Experiences with point-mass gravity field modelling in the Perth region, *Geomatics Res. Australas.*, **75**, 53–86.
- Clenshaw, C.W., 1955. A note on the summation of Chebyshev series, *Math. Comput.*, **9**, 118–120.
-   nderl  k, R., Mikula, K. & Mojze  , M., 2008. Numerical solution of the linearized fixed gravimetric boundary-value problem, *J. Geod.*, **82**, 15–29.
- Driscoll, J.R. & Healy, D.M., 1994. Computing Fourier transforms and convolutions on the 2-sphere, *Adv. Appl. Math.*, **15**, 202–250.
- Eicker, A., 2008. Gravity field refinement by radial basis functions from in-situ satellite data, *PhD thesis*, Universit  t Bonn, Bonn, Germany, 137 pp.
- Eicker, A., Schall, J. & Kusche, J., 2014. Regional gravity modelling from spaceborne data: case studies with GOCE, *Geophys. J. Int.*, **196**, 1431–1440.
- Elhabiby, M., Sampietro, D., Sans  , F. & Siders, M.G., 2009. BVP, global models and residual terrain correction, in *Observing our Changing Earth: Proceedings of the 2007 IAG General Assembly*, Perugia, July 2–13, Italy, Vol. 133, pp. 211–217, Springer-Verlag, Berlin.
- Fantino, E. & Casotto, S., 2009. Methods of harmonic synthesis for global geopotential models and their first-, second- and third-order gradients, *J. Geod.*, **83**, 595–619.
- Fa  kov  , Z.,   nderl  k, R. & Mikula, K., 2010. Finite element method for solving geodetic boundary value problems, *J. Geod.*, **84**, 135–144.
- Fornberg, B., 1988. Generation of finite difference formulas on arbitrarily spaced grids, *Math. Comput.*, **51**, 699–706.
- Forsberg, R., 1984. A study of terrain reductions, density anomalies and geophysical inversion methods in gravity field modelling, Report No. 355, Department of Geodetic Science and Surveying, The Ohio State University, Columbus, Ohio, 129 pp.
- F  rste, C. et al., 2014. EIGEN-6C4 The latest combined global gravity field model including GOCE data up to degree and order 2190 of GFZ Potsdam and GRGS Toulouse, in *5th GOCE User Workshop*, Paris, France, 25–28 November.
- Freed, W. & Schneider, F., 1998. An integrated wavelet concept of physical geodesy, *J. Geod.*, **72**, 259–281.
- Freed, W. & Schreiner, M., 2009. *Spherical Functions of Mathematical Geosciences: A Scalar, Vectorial, and Tensorial Setup*, Springer-Verlag, 602 pp.
- Freed, W. & Windheuser, U., 1997. Combined spherical harmonic and wavelet expansion—a future concept in Earth's gravitational determination, *Appl. Comput. Harmon. Anal.*, **4**, 1–37.
- Freed, W., Gervens, T. & Schreiner, M., 1998. *Constructive Approximation on the Sphere: With Applications to Geomathematics*, Clarendon Press, 427 pp.
- Fukushima, T., 2012. Numerical computation of spherical harmonics of arbitrary degree and order by extending exponent of floating point numbers, *J. Geod.*, **86**, 271–285.
- Gilardoni, M., Reguzzoni, M. & Sampietro, D., 2016. GECO: a global gravity field model by locally combining GOCE data and EGM2008, *Stud. Geophys. Geod.*, **60**, 228–247.
- Grombein, T., Seitz, K. & Heck, B., 2013. Optimized formulas for the gravitational field of a tesseroid, *J. Geod.*, **87**, 645–660.
- Gruber, C., Nov  k, P. & Sebera, J., 2011. FFT-based high-performance spherical harmonic transformation, *Stud. Geophys. Geod.*, **55**, 489–500.
- Hirt, C., 2010. Prediction of vertical deflections from high-degree spherical harmonic synthesis and residual terrain model data, *J. Geod.*, **84**, 179–190.
- Hirt, C. & Kuhn, M., 2014. Band-limited topographic mass distribution generates full-spectrum gravity field: gravity forward modeling in the spectral and spatial domains revisited, *J. Geophys. Res.*, **119**, 3646–3661.
- Hirt, C. & Rexer, M., 2015. Earth2014: 1 arc-min shape, topography, bedrock and ice-sheet models - available as gridded data and degree-10,800 spherical harmonics, *Int. J. Appl. Earth Obs. Geoinf.*, **39**, 103–112.
- Hirt, C., Featherstone, W.E. & Marti, U., 2010. Combining EGM2008 and SRTM/DTM2006.0 residual terrain model data to improve quasigeoid computations in mountainous areas devoid of gravity data, *J. Geod.*, **84**, 557–567.
- Hirt, C., Kuhn, M., Claessens, S., Pail, R., Seitz, K. & Gruber, T., 2014. Study of the Earth's short-scale gravity field using the ERTM2160 gravity model, *Comput. Geosci.*, **73**, 71–80.
- Hoffmann-Wellenhof, B. & Moritz, H., 2005. *Physical Geodesy*, Springer, 403 pp.
- Jekeli, C., 1999. An analysis of vertical deflections derived from high-degree spherical harmonic models, *J. Geod.*, **73**, 10–22.
- Jekeli, C., 2005. Spline representations of functions on a sphere for geopotential modeling, Report No. 475, Department of Civil and Environmental Engineering and Geodetic Science, The Ohio State University, Columbus, Ohio, 34 pp.
- Jekeli, C. & Zhu, L., 2006. Comparison of methods to model the gravitational gradients from topographic data bases, *Geophys. J. Int.*, **166**, 999–1014.
- Kadlec, M., 2011. Refining gravity field parameters by residual terrain modelling, *PhD thesis*, University of West Bohemia, Pilsen, Czech Republic, 150 pp.
- Kaula, W.M., 1966. *Theory of Satellite Geodesy: Applications of Satellites to Geodesy*, Blaisdell, 124 pp.
- Klees, R., Tenzer, R., Prutkin, I. & Wittner, T., 2008. A data-driven approach to local gravity field modelling using spherical radial basis functions, *J. Geod.*, **82**, 457–471.
- Koch, K.R. & Kusche, J., 2002. Regularization of geopotential determination from satellite data by variance components, *J. Geod.*, **76**, 259–268.
- Koop, R. & Stelpstra, D., 1989. On the computation of the gravitational potential and its first and second order derivatives, *Manuscr. Geod.*, **14**, 373–382.
- Krarup, T., 1969. A contribution to the mathematical foundation of physical geodesy, Meddelelse No. 44, Geod  tisk Institut, K  benhavn.
- Kube  , P., Grand, T.,   efara, J., Pa  teka, R., Bielik, M. & Daniel, S., 2001. Atlas of geophysical maps and profiles: D1 - part gravimetry, Final Report 0801840301/180, State Geological Institute of Dion  z   t  r, Bratislava, Slovak Republic, 67 pp. (in Slovak).
- Kuroishi, Y. & Keller, W., 2005. Wavelet approach to improvement of gravity field—geoid modeling for Japan, *J. Geophys. Res.*, **110**, B03402, doi:10.1029/2004JB003371.
- Kusche, J., 2003. A Monte-Carlo technique for weight estimation in satellite geodesy, *J. Geod.*, **76**, 641–652.
- Lin, M., Denker, H. & M  ller, J., 2014. Regional gravity field modeling using free-positioned point masses, *Stud. Geophys. Geod.*, **58**, 207–226.
- Mac  k, M., Minarechov  , Z. & Mikula, K., 2014. A novel scheme for solving the oblique derivative boundary-value problem, *Stud. Geophys. Geod.*, **58**, 556–570.
- Mojze  , M., Czarnecki, K., Hus  r, L., Jan  k, J., Bogusz, J., Pap  o, J., Val  ko, M. & Walo, J., 2006. Using of deflections of the vertical for testing of gravimetric quasigeoid in the mountains, *Geophysical Research Abstracts*, Vol. 8, 08909.

- Moritz, H., 1980. *Advanced Physical Geodesy*, Herbert Wichmann Verlag, 500 pp.
- Moritz, H., 2000. Geodetic reference system 1980, *J. Geod.*, **74**, 128–133.
- Naeimi, M., 2013. Inversion of satellite gravity data using spherical radial base functions, *PhD thesis*, Leibniz Universität Hannover, Hannover, Germany, 130 pp.
- Naeimi, M., Flury, J. & Brieden, P., 2015. On the regularization of regional gravity field solutions in spherical radial base functions, *Geophys. J. Int.*, **202**, 1041–1053.
- Omang, O.C., Tscherning, C.C. & Forsberg, R., 2012. Generalizing the harmonic reduction procedure in residual topographic modeling, in *VII Hotine-Marussi Symposium on Mathematical Geodesy: Proceedings of the Symposium in Rome*, 6–10 June, 2009, IAG Symposia, Vol. 137, pp. 233–238, Springer-Verlag, Berlin.
- Panet, I., Kuroishi, Y. & Holschneider, M., 2011. Wavelet modelling of the gravity field by domain decomposition methods: an example over Japan, *Geophys. J. Int.*, **184**, 203–219.
- Pavlis, N.K., Factor, J.K. & Holmes, S.A., 2007. Terrain-related gravimetric quantities computed for the next EGM, in *Proceedings of the 1st International Symposium of the International Gravity Field Service*, Vol. 18, pp. 318–323, Harita Dergisi, Istanbul.
- Pavlis, N.K., Holmes, S.A., Kenyon, S.C. & Factor, J.K., 2012. The development and evaluation of the Earth Gravitational Model 2008 (EGM2008), *J. geophys. Res.*, **117**, B04406. doi:10.1029/2011JB008916.
- Pašteka, R. et al., 2014. Recalculation of regional and detailed gravity database from Slovak Republic and qualitative interpretation of new generation Bouguer anomaly map, *Geophysical Research Abstracts*, Vol. 16, 9439.
- Pock, C., Mayer-Guerr, T. & Kuehtreiber, N., 2014. Consistent combination of satellite and terrestrial gravity field observations in regional geoid modeling: a case study for Austria, in *Gravity, Geoid and Height Systems: Proceedings of the IAG Symposium GGHS2012*, October 9–12, 2012, Venice, Italy, Vol. 141, pp. 151–156, Springer, International Publishing Switzerland.
- Reuter, R., 1982. Über integralformeln der einheitsphäre und harmonische splinefunktionen, Heft Nr. 33, Veröff. Geod. Inst. RWTH Aachen, Germany.
- Rexer, M. & Hirt, C., 2015a. Spectral analysis of the Earth's topographic potential via 2D-DFT: a new data-based degree variance model to degree 90,000, *J. Geod.*, **89**, 887–909.
- Rexer, M. & Hirt, C., 2015b. Ultra-high-degree surface spherical harmonic analysis using the Gauss–Legendre and the Driscoll/Healy quadrature theorem and application to planetary topography models of Earth, Mars and Moon, *Surv. Geophys.*, **36**, 803–830.
- Sansò, F. & Sideris, M.G., 2013. *Geoid Determination: Theory and Methods*, Springer, 734 pp.
- Schmidt, M., Fabert, O. & Shum, C.K., 2005. On the estimation of a multi-resolution representation of the gravity field based on spherical harmonics and wavelets, *J. Geodyn.*, **39**, 512–526.
- Schmidt, M., Fengler, M., Mayer-Gürr, T., Eicker, A., Kusche, J., Sánchez, L. & Han, S.-C., 2007. Regional gravity modeling in terms of spherical base functions, *J. Geod.*, **81**, 17–38.
- Sebera, J., Wagner, C.A., Bezděk, A. & Klokočník, J., 2013. Short guide to direct gravitational field modelling with Hotine's equations, *J. Geod.*, **87**, 223–238.
- Sjöberg, L.E. & Hunegnaw, A., 2000. Some modifications of Stokes' formula that account for truncation and potential coefficients errors, *J. Geod.*, **74**, 232–238.
- Sneeuw, N., 1994. Global spherical harmonic analysis by least-squares and numerical quadrature methods in historical perspective, *Geophys. J. Int.*, **118**, 707–716.
- Šprlák, M., 2008. Numerical testing of procedures for the determination of the quasigeoid, *PhD thesis*, Slovak University of Technology in Bratislava, Bratislava, Slovakia, 150 pp. (in Slovak).
- Tenzer, R. & Klees, R., 2008. The choice of the spherical radial basis functions in local gravity field modeling, *Stud. Geophys. Geod.*, **52**, 287–304.
- Tenzer, R., Klees, R. & Wittwer, T., 2012. Local gravity field modelling in rugged terrain using spherical radial basis functions: case study for the Canadian Rocky Mountains, in *Geodesy for Planet Earth: Proceedings of the 2009 IAG Symposium*, Vol. 136, pp. 401–409, Buenos Aires, Argentina.
- Tikhonov, A.N. & Arsenin, V.Y., 1977. *Solutions of Ill-posed Problems*, Wiley.
- Tscherning, C.C., 1976a. On the chain-rule method for computing potential derivatives, *Manuscr. Geod.*, **1**, 125–141.
- Tscherning, C.C., 1976b. Covariance expressions for second and lower order derivatives of the anomalous potential, Report No. 255, Department of Geodetic Science, The Ohio State University, Ohio, USA, 62 pp.
- Tscherning, C.C., 1993. Computation of covariances of derivatives of the anomalous gravity potential in a rotated reference frame, *Manuscr. Geod.*, **18**, 115–123.
- Tscherning, C.C. & Poder, K., 1982. Some geodetic applications of Clenshaw summation, *Bollettino di Geodesia e Scienze Affini*, **XLI**, 349–375.
- Tsoulis, D., 2003. Terrain modeling in forward gravimetric problems: a case study on local terrain effects, *J. Appl. Geophys.*, **54**, 145–160.
- Tsoulis, D., 2012. Analytical computation of the full gravity tensor of a homogeneous arbitrarily shaped polyhedral source using line integrals, *Geophysics*, **77**, F1–F11.
- Vařko, M., Mojzeš, M., Janák, J. & Papčo, J., 2008. Comparison of two different solutions to Molodensky's G_1 term, *Stud. Geophys. Geod.*, **52**, 71–86.
- Weightman, J.A., 1967. Gravity, geodesy and artificial satellites. A unified analytical approach, in *The Use of Artificial Satellites for Geodesy*, Vol. 2, pp. 467–486, ed. Veis, G., National Technical University of Athens.
- Wessel, P. & Smith, W.H.F., 1998. New, improved version of generic mapping tools released, *EOS, Trans. Am. Geophys. Un.*, **79**, 579, doi: 10.1029/98EO00426.
- Wittwer, T., 2009. Regional gravity field modelling with radial basis functions, *PhD thesis*, Delft University of Technology, Delft, the Netherlands, 191 pp.
- Zahorec, P., Papčo, J., Mikolaj, M., Pašteka, R. & Szalaiová, V., 2014. The role of near topography and building effects in vertical gravity gradients approximation, *First Break*, **32**, 65–71.

APPENDIX: SECOND-ORDER DERIVATIVES OF SPHERICAL RADIAL BASIS FUNCTIONS

Several approaches to compute the second-order derivatives of SRBFs in Cartesian coordinates are available in the literature (e.g. Tscherning 1976b, 1993; Eicker 2008). In the LNOFs, the following relations are valid (Koop & Stelpstra 1989),

$$\begin{aligned}\Phi_{xx} &= \frac{1}{r} \Phi_r + \frac{1}{r^2} \Phi_{\varphi\varphi}, \\ \Phi_{xy} &= -\frac{1}{r^2 \cos \varphi} \Phi_{\varphi\lambda} - \frac{1}{r^2 \cos \varphi} \tan \varphi \Phi_\lambda, \\ \Phi_{xz} &= \frac{1}{r} \Phi_{r\varphi} - \frac{1}{r^2} \Phi_\varphi, \\ \Phi_{yy} &= \frac{1}{r} \Phi_r - \frac{1}{r^2} \tan \varphi \Phi_\varphi + \frac{1}{r^2 \cos^2 \varphi} \Phi_{\lambda\lambda}, \\ \Phi_{yz} &= -\frac{1}{r \cos \varphi} \Phi_{r\lambda} + \frac{1}{r^2 \cos \varphi} \Phi_\lambda, \\ \Phi_{zz} &= \Phi_{rr},\end{aligned}\tag{A1}$$

where r, φ, λ denote the spherical radius, the spherical latitude and the longitude, respectively.

The first-order partial derivatives in eq. (A1) read

$$\begin{aligned}\Phi_r &= -\frac{1}{R} \sum_{n=n_{\min}}^{n_{\max}} k_n (n+1) \left(\frac{R}{r}\right)^{n+2} P_n(\cos \psi), \\ \Phi_\varphi &= -\cos \alpha \sum_{n=n_{\min}}^{n_{\max}} k_n \left(\frac{R}{r}\right)^{n+1} \frac{dP_n(\cos \psi)}{d\psi}, \\ \Phi_\lambda &= -\sin \alpha \cos \varphi \sum_{n=n_{\min}}^{n_{\max}} k_n \left(\frac{R}{r}\right)^{n+1} \frac{dP_n(\cos \psi)}{d\psi},\end{aligned}\quad (\text{A2})$$

where we used the substitution $k_n = (2n+1)/(4\pi R^2) \phi_n$. To obtain the two formulae for Φ_φ and Φ_λ , the latitudinal and longitudinal derivatives of Legendre polynomials need to be derived (see e.g. section 2.19 of Hoffmann-Wellenhof & Moritz 2005),

$$\begin{aligned}\frac{\partial P_n(\cos \psi)}{\partial \varphi} &= -\cos \alpha \frac{dP_n(\cos \psi)}{d\psi}, \\ \frac{\partial P_n(\cos \psi)}{\partial \lambda} &= -\sin \alpha \cos \varphi \frac{dP_n(\cos \psi)}{d\psi},\end{aligned}\quad (\text{A3})$$

with α being the azimuth between P and P' .

The second-order derivatives with respect to the radius r and subsequently r, φ, λ follow immediately from eq. (A2),

$$\begin{aligned}\Phi_{rr} &= \frac{1}{R^2} \sum_{n=n_{\min}}^{n_{\max}} k_n (n+1)(n+2) \left(\frac{R}{r}\right)^{n+3} P_n(\cos \psi), \\ \Phi_{r\varphi} &= \frac{\cos \alpha}{R} \sum_{n=n_{\min}}^{n_{\max}} k_n (n+1) \left(\frac{R}{r}\right)^{n+2} \frac{dP_n(\cos \psi)}{d\psi}, \\ \Phi_{r\lambda} &= \frac{\sin \alpha \cos \varphi}{R} \sum_{n=n_{\min}}^{n_{\max}} k_n (n+1) \left(\frac{R}{r}\right)^{n+2} \frac{dP_n(\cos \psi)}{d\psi}.\end{aligned}\quad (\text{A4})$$

To derive the three remaining second-order derivatives, we recall a few relations from spherical trigonometry (ibid.),

$$\cos \psi = \sin \varphi \sin \varphi' + \cos \varphi \cos \varphi' \cos(\lambda' - \lambda), \quad (\text{A5})$$

$$\sin \psi \cos \alpha = \cos \varphi \sin \varphi' - \sin \varphi \cos \varphi' \cos(\lambda' - \lambda), \quad (\text{A6})$$

$$\sin \psi \sin \alpha = \cos \varphi' \sin(\lambda' - \lambda), \quad (\text{A7})$$

$$\tan \alpha = \frac{\cos \varphi' \sin(\lambda' - \lambda)}{\cos \varphi \sin \varphi' - \sin \varphi \cos \varphi' \cos(\lambda' - \lambda)} \quad (\text{A8})$$

as well as the partial derivatives of the spherical distance (ibid.),

$$\frac{\partial \psi}{\partial \varphi} = -\cos \alpha, \quad \frac{\partial \psi}{\partial \lambda} = -\cos \varphi \sin \alpha. \quad (\text{A9})$$

With the help of eqs (A5)–(A9) and after some manipulations, we have

$$\begin{aligned}\frac{\partial^2 P_n(\cos \psi)}{\partial \varphi^2} &= \frac{d^2 P_n(\cos \psi)}{d\psi^2} \left(\frac{\partial \psi}{\partial \varphi}\right)^2 + \frac{dP_n(\cos \psi)}{d\psi} \frac{\partial^2 \psi}{\partial \varphi^2} \\ &= \frac{d^2 P_n(\cos \psi)}{d\psi^2} \cos^2 \alpha \\ &\quad + \frac{dP_n(\cos \psi)}{d\psi} \frac{\cos \psi (1 - \cos^2 \alpha)}{\sin \psi},\end{aligned}\quad (\text{A10})$$

where the term $\partial^2 \psi / \partial \varphi^2$ is derived by double differentiation of eq. (A5) with respect to φ . Similarly, we get

$$\begin{aligned}&\frac{\partial^2 P_n(\cos \psi)}{\partial \varphi \partial \lambda} \\ &= \frac{\partial^2 P_n(\cos \psi)}{\partial \lambda \partial \varphi} = \frac{\partial}{\partial \lambda} \left(\frac{dP_n(\cos \psi)}{d\psi} \frac{\partial \psi}{\partial \varphi} \right) \\ &= \frac{d^2 P_n(\cos \psi)}{d\psi^2} \frac{\partial \psi}{\partial \lambda} (-\cos \alpha) + \frac{dP_n(\cos \psi)}{d\psi} \frac{\partial \alpha}{\partial \lambda} \sin \alpha \\ &= \frac{d^2 P_n(\cos \psi)}{d\psi^2} \cos \varphi \sin \alpha \cos \alpha + \frac{dP_n(\cos \psi)}{d\psi} \\ &\quad \times \cos \varphi' \sin \alpha \frac{\sin \varphi \sin(\lambda' - \lambda) \sin \alpha - \cos(\lambda' - \lambda) \cos \alpha}{\sin \psi},\end{aligned}\quad (\text{A11})$$

with $\partial \alpha / \partial \lambda$ being obtained from eq. (A8). And finally,

$$\begin{aligned}\frac{\partial^2 P_n(\cos \psi)}{\partial \lambda^2} &= \frac{d^2 P_n(\cos \psi)}{d\psi^2} \left(\frac{\partial \psi}{\partial \lambda}\right)^2 + \frac{dP_n(\cos \psi)}{d\psi} \frac{\partial^2 \psi}{\partial \lambda^2} \\ &= \frac{d^2 P_n(\cos \psi)}{d\psi^2} \sin^2 \alpha \cos^2 \varphi + \frac{dP_n(\cos \psi)}{d\psi} \\ &\quad \times \frac{\cos \psi (1 - \sin^2 \alpha \cos^2 \varphi) - \sin \varphi \sin \varphi'}{\sin \psi},\end{aligned}\quad (\text{A12})$$

where $\partial^2 \psi / \partial \lambda^2$ is derived from eq. (A5). Using eqs (A10)–(A12), we obtain

$$\begin{aligned}\Phi_{\varphi\varphi} &= \sum_{n=n_{\min}}^{n_{\max}} k_n \left(\frac{R}{r}\right)^{n+1} \left[\frac{d^2 P_n(\cos \psi)}{d\psi^2} \cos^2 \alpha \right. \\ &\quad \left. + \frac{dP_n(\cos \psi)}{d\psi} \frac{\cos \psi (1 - \cos^2 \alpha)}{\sin \psi} \right], \\ \Phi_{\varphi\lambda} &= \sum_{n=n_{\min}}^{n_{\max}} k_n \left(\frac{R}{r}\right)^{n+1} \left[\frac{d^2 P_n(\cos \psi)}{d\psi^2} \cos \varphi \sin \alpha \cos \alpha \right. \\ &\quad \left. + \frac{dP_n(\cos \psi)}{d\psi} \cos \varphi' \sin \alpha \right. \\ &\quad \left. \times \frac{\sin \varphi \sin(\lambda' - \lambda) \sin \alpha - \cos(\lambda' - \lambda) \cos \alpha}{\sin \psi} \right], \\ \Phi_{\lambda\lambda} &= \sum_{n=n_{\min}}^{n_{\max}} k_n \left(\frac{R}{r}\right)^{n+1} \left[\frac{d^2 P_n(\cos \psi)}{d\psi^2} \sin^2 \alpha \cos^2 \varphi \right. \\ &\quad \left. + \frac{dP_n(\cos \psi)}{d\psi} \frac{\cos \psi (1 - \sin^2 \alpha \cos^2 \varphi) - \sin \varphi \sin \varphi'}{\sin \psi} \right].\end{aligned}\quad (\text{A13})$$

In these equations, each product with the term $dP_n(\cos \psi)/d\psi = P'_n(t)$ in it takes the indeterminate form $0/0$ for $\psi = 0$. Using

de l'Hôpital's rule, we find that the limits of these products for $\psi \rightarrow 0$ are equal to the original products, but with $\cos \psi = 1$ in the denominators and with $P_n''(t)$ instead of $P_n'(t)$. Therefore, when programming eqs (A13), it is beneficial to introduce modified Legendre polynomials $\hat{P}_n(t)$, being equal to $P_n''(t)$ for $\psi = 0$ and to $P_n'(t)/\sin \psi$ otherwise. These can be obtained by modifying the original recursions for $P_n'(t)$

$$\begin{aligned} P_n'(t) &= (2n - 1)t' P_{n-1}(t) + P_{n-2}'(t), \quad n \geq 2 \\ P_0'(t) &= 0, \quad P_1'(t) = t' \end{aligned} \quad (\text{A14})$$

to the form

$$\begin{aligned} \hat{P}_n'(t) &= -(2n - 1)P_{n-1}(t) + \hat{P}_{n-2}'(t), \quad n \geq 2 \\ \hat{P}_0'(t) &= 0, \quad \hat{P}_1'(t) = -1. \end{aligned} \quad (\text{A15})$$

The final expression for $\Phi_{\varphi\varphi}$, valid and numerically stable for each ψ , thus reads

$$\begin{aligned} \Phi_{\varphi\varphi} = \sum_{n=n_{\min}}^{n_{\max}} k_n \left(\frac{R}{r}\right)^{n+1} &\left[\frac{d^2 P_n(\cos \psi)}{d\psi^2} \cos^2 \alpha \right. \\ &\left. + \frac{d\hat{P}_n(\cos \psi)}{d\psi} \cos \psi (1 - \cos^2 \alpha) \right]. \end{aligned} \quad (\text{A16})$$

The modified formulae for $\Phi_{\varphi\lambda}$ and $\Phi_{\lambda\lambda}$ can be derived in a similar manner.

The second-order derivatives in the LNOFs are obtained by substituting eqs (A2), (A4) and the numerically stable form of eq. (A13) into eq. (A1). Recursions for $P(t)$, $P'(t)$ and $P''(t)$ can be found, for example, in Tscherning (1976a).